CELL BIOLOGY

SpotMAX: A generalist framework for multidimensional automatic spot detection and quantification

Francesco Padovani[1]*, Ivana Čavka[2,3], Ana Rita Rodrigues Neves[2,3], Cristina Piñeiro López[2], Nada Al-Refaie[1,4], Leonardo Bolcato[1], Dimitra Chatzitheodoridou[1], Yagya Chadha[1], Pablo Lagos[2,3], Timon Stegmaier[1], Xiaofeng A. Su[5], Jette Lengefeld[6,7], Daphne S. Cabianca[1], Simone Köhler[2]*, Kurt M. Schmoller[1]*

The analysis of spot-like structures is a widespread task in microscopy image analysis. Existing solutions are typically specific to single applications and do not use multidimensional information, often leaving manual annotation as the only option. Here, we present SpotMAX, a generalist AI-assisted framework for automated spot detection and quantification. SpotMAX detects spots in three-dimensional (3D) data and leverages the full scope of multidimensional datasets with an easy-to-use graphical user interface and a framework for cell segmentation and tracking. Tested on a large 3D dataset, SpotMAX outperforms or is on par with state-of-the-art tools and expert human annotators. We applied SpotMAX across diverse experimental questions, ranging from meiotic crossover events in *Caenorhabditis elegans* to mitochondrial DNA dynamics in *Saccharomyces cerevisiae* and telomere length in mouse stem cells, leading to new biological insights. With its flexibility in integrating other AI models into a holistic analysis workflow, we anticipate that SpotMAX will become the standard for spot analysis in microscopy data.

INTRODUCTION

Spot-like structures are a ubiquitous feature in fluorescence microscopy data, and their analysis is a fundamental task in bioimage analysis. However, no generalist gold-standard tool for spot detection and quantification exists. Microscopy image analysis has seen a revolution with the advent of artificial intelligence (AI)–based workflows, but spot detection and quantification have not fully taken advantage of this potential. Current state-of-the-art (SOTA) tools are mainly developed for detecting diffraction-limited RNA transcripts from single-molecule fluorescence in situ hybridization (FISH) data or similar approaches, including imaging-based spatial transcriptomics (*1*–*10*). These tools are often limited to spot detection, leaving the quantification of spot features, such as their size and intensities, as a downstream process to be implemented separately. Furthermore, microscopy data is often multidimensional, where the spot analysis must be performed in the multichannel context or requires 3D detection and the ability to go beyond single time-point detection. Some of the most recent SOTA tools implement advanced AI-based workflows (*2*, *6*, *7*, *9*), but they mostly remain limited to detection in two-dimensions (2D), and none of the existing tools covers all aspects required for the rigorous analysis of spots in 5D microscopy data. This makes it hard for experimentalists to find an appropriate tool because integrating the multidimensional information requires advanced technical knowledge. In many cases, manual detection remains the only viable method for experimental biologists, a strategy that can be extremely tedious and time-consuming, potentially introducing mistakes due to human bias. Therefore, a standard tool for generalist spot detection and quantification of 3D globular-like structures with support for time-lapse data is urgently needed.

To solve these issues, we developed SpotMAX (spot detection by local MAX search), a generalist spot detection and quantification framework for multidimensional microscopy data. SpotMAX provides an easy-to-use unified framework to combine AI-driven spot detection workflows with additional downstream interpretable analysis. It harnesses all the relevant information available in multidimensional datasets, such as single-cell segmentation masks, reference channels (e.g., separate staining of the cell nucleus), and multidimensionality such as z-slices and time lapse. We developed SpotMAX with three main objectives: (i) providing better performance than existing SOTA tools, (ii) enabling experimental biologists to uncover new biological insights, and (iii) making it easy to use from a graphical user interface without specialist programming knowledge. First, to assess the accuracy of spot detection with SpotMAX, we manually annotated a large 3D dataset of experimental data, which can also serve as a powerful resource for training and validating 3D spot detection models. Since such a resource was missing, we made the dataset available to the community. Next, we extensively benchmarked SpotMAX and found that it achieves performance comparable to, and in many cases exceeding, that of SOTA tools, nonexpert annotators, and, in some cases, even expert annotators.

Moreover, when spot counting alone is not sufficient, further quantification and information from additional channels are required. To achieve this, SpotMAX provides a framework for automatic segmentation of the reference structures and quantifying several spot features, such as their size, intensities, and signal-to-noise ratio (SNR). To test SpotMAX in real-world scenarios, we applied SpotMAX to multiple imaging modalities, model organisms, biological questions, and experimental protocols. This included the quantification of crossover events in *Caenorhabditis elegans* meiosis, multigenerational dynamics

[1]Institute of Functional Epigenetics, Molecular Targets and Therapeutics Center, Helmholtz Zentrum München, Neuherberg, Germany. [2]Cell Biology and Biophysics Unit, European Molecular Biology Laboratory, Heidelberg, Baden-Württemberg, Germany. [3]Collaboration for joint PhD degree between EMBL and Heidelberg University, Faculty of Biosciences, Heidelberg University, Heidelberg, Baden-Württemberg, Germany. [4]Faculty of Medicine, Ludwig-Maximilians Universität München, Munich, Germany. [5]David H. Koch Institute for Integrative Cancer Research, and Department of Biology, Massachusetts Institute of Technology, Cambridge, MA 02139, USA. [6]Helsinki Institute of Life Science, Institute of Biotechnology, Faculty of Biological and Environmental Sciences, University of Helsinki, Helsinki, Finland. [7]Centre for Hematology and Regenerative Medicine, Department of Medicine Huddinge, Karolinska Institutet, Huddinge, Sweden.
*Corresponding author. Email: francesco.padovani@helmholtz-munich.de (F.P.); simone.koehler@embl.de (S.K.); kurt.schmoller@helmholtz-munich.de (K.M.S.)

of mitochondrial DNA (mtDNA) adaptation in response to a nutrient shift in *Saccharomyces cerevisiae*, telomere length as a function of cell size in hematopoietic stem cells (HSCs), and Raptor depletion effects on the nucleus and nucleolus size in *C. elegans*. For each application, we demonstrated that by leveraging multidimensionality and extracting biologically meaningful features, SpotMAX can reveal new biological insights.

SpotMAX is available to the community as open-source software as a plugin of Cell-ACDC (*11*), a command line interface, and as a Python package with extensive documentation (see links below). The command-line interface enables SpotMAX to easily scale to high-throughput analysis in high-performance computing environments. Crucially, we provide an intuitive and user-friendly graphical user interface (GUI) integrated into the Cell-ACDC software, which already provides a comprehensive framework for object segmentation (e.g., 2D or 3D cell segmentation). When suitable, analysis steps can be performed with any of the models available on the BioImage.IO model zoo (*12*), streamlining integration with existing and future strategies.

Thanks to its superior performance, ease of use, and high accessibility, we envision SpotMAX to become a standard for general fluorescence spot detection and quantification tasks in biological research (documentation: https://spotmax.readthedocs.io/en/latest/index.html; source code: https://github.com/SchmollerLab/SpotMAX).

RESULTS

Software architecture

Microscopy data with spot-like features are often multidimensional, including multiple channels that typically represent cells or entities containing spot-like structures. To assign the detected spots and structures in the reference channel to the parent objects, SpotMAX requires segmentation masks of these objects. These masks can be generated directly in Cell-ACDC (*11*), where SpotMAX can be run as a plugin. Alternatively, the masks can be obtained with any segmentation software and provided to SpotMAX as input.

SpotMAX is composed of the following modules: (i) preprocessing input images, (ii) optional semantic segmentation of the reference channel, (iii) reference channel quantification, (iv) semantic segmentation of the spots channel, (v) spot detection, and (vi) spot quantification and validation loop (Fig. 1). These modules run sequentially, and, if needed, the input of each module can be replaced by the output of external software. This modularity facilitates a high degree of integration with existing or future methods.

The reference channel segmentation is performed in two steps: (i) image preprocessing (module 1) and (ii) semantic segmentation (module 2). For image preprocessing, two filters can be applied: a Gaussian smoothing filter and a filter that enhances network-like structures (*13*). For the semantic segmentation, either automatic thresholding or any of the models available at the BioImage.IO (*12*) model zoo can be applied. Once segmented, reference channel objects are identified via connected-component labeling and, if a segmentation mask is provided as input, assigned to the parent objects (e.g., cells) they belong to. Last, several numerical quantities—such as intensities, size, and morphological features—of the reference channel are computed in module 3.

For the semantic segmentation of the spots channel (module 4), the z-stack image can be preprocessed with a spot detection filter (difference of Gaussians), whose parameters are determined from the expected spot size (see Materials and Methods). The filtered image is then used as input into four possible strategies: (i) automatic thresholding, (ii) SpotMAX AI, (iii) Spotiflow (*2*), or (iv) any model of the BioImage.IO model zoo. The SpotMAX AI consists of 2D or 3D U-Net–based neural networks (fig. S1) that we trained to perform semantic segmentation of the spots channel. The training data consisted of manually annotated 3D diffraction-limited spots from single-molecule FISH (*14*, *15*), mtDNA nucleoid data (*16*), and publicly available 2D datasets (*6*).

To separate the spots merged in the semantic segmentation mask and detect their center (module 5), SpotMAX performs local peak detection with a footprint determined from the expected spot size. For diffraction-limited spots, the expected spot size is calculated automatically from the image acquisition parameters (see Materials and Methods). For larger spots, the spot size can be visually adjusted in the GUI.

To quantify spot features (module 6), SpotMAX uses the pixels of a spheroid mask with an expected spot size centered at the spot center. These features include several intensity distribution metrics (mean, max, median, quantiles, etc.) from the raw, Gaussian-filtered, and DoG-filtered images, including different background correction strategies.

Spots can also be further quantified with a Gaussian peak fitting procedure (SpotFIT, module 6). We optimized this procedure for high-density spots where multiple spots are fitted together with a sum of 3D (or 2D) Gaussian functions (see Materials and Methods). The SpotFIT framework computes additional features, including the total integral of the Gaussian function, the size of the spot, the amplitude, and the background level.

SpotMAX matches or exceeds the performance of SOTA methods and experienced human annotators across the evaluated datasets

To evaluate the performance of SpotMAX in experimental datasets, we designed several benchmarks with realistic simulations of the typical annotation process faced by experimental biologists (Fig. 2). While several high-performance tools for 2D detection exist, many applications require analysis of 3D data. One typical workaround for this is to detect spots from 2D projections of 3D data, a practice that can introduce counting errors (due to overlapping spots). Since a key advantage of SpotMAX is the ability to detect spots in 3D z-stack data, we focused on 3D datasets. Because a high-quality 3D ground truth dataset did not exist so far, we asked expert annotators to annotate the spot centers in the following 3D datasets: (i) single-molecule RNA FISH in *S. cerevisiae,* (ii) mtDNA nucleoids in *S. cerevisiae*, and (iii) chromosomal crossovers (COs) in the multicellular organism *C. elegans.* All annotations were performed using Cell-ACDC (*11*). We generated a ground truth dataset of 369 volumes with 20,692 annotated spots from 2894 cells, including 1060 cells without true positives (models were allowed to detect false positives on these cells). Each category has a different pixel size, experimental protocol, and imaging method; therefore, we stratified the results based on these three categories. We also performed additional stratification by the SNR (fig. S2). Details about the ground truth datasets are available in Materials and Methods and table S1. Next, we selected SOTA tools—that span from deep learning–based to classical algorithms—to benchmark against SpotMAX. The tested tools are (i) RS-FISH (*1*), (ii) Spotiflow (*2*), (iii) Big-FISH (FISH-quant v2) (*3*), U-FISH (*9*), Piscis (*7*), and—in spot detection benchmarks—(iii) expert manual counting (human). For a fair comparison, in Fig. 2, with SpotMAX we did not use the trained U-Net but the automatic thresholding

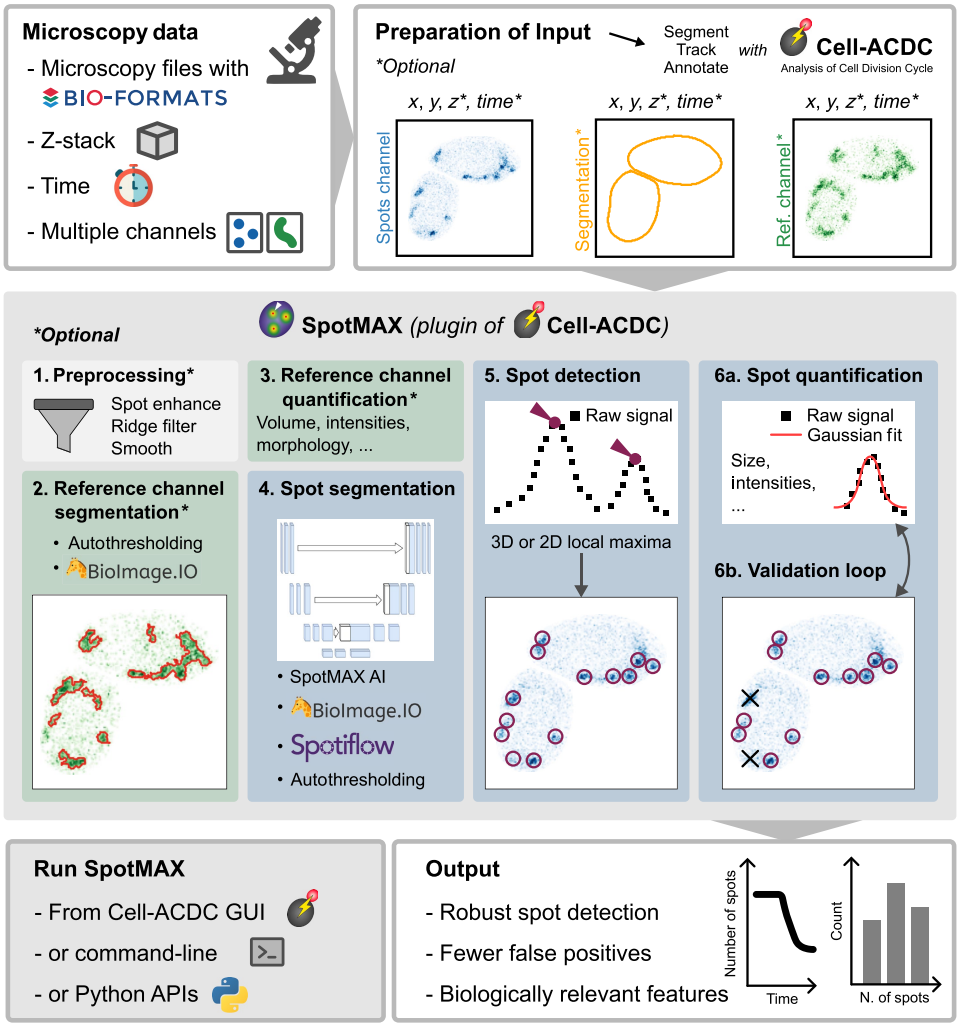

Fig. 1. Schematic overview of the SpotMAX framework. SpotMAX leverages the multidimensionality of microscopy datasets, including time, z-slices, additional channels that provide information about the localization of the spots (a reference channel), and segmentation masks. The single cells can be segmented, tracked, and mother-daughter relationships can be annotated with Cell-ACDC (*11*) or any other external software. The input images plus segmentation masks go through a series of optional filters designed to enhance the structure of interest. The preprocessed images are then fed to the prediction step, where automatic thresholding or AI-based models can be used to generate binary masks for both the spots and reference channels. These models include custom-designed 2D or 3D U-Net models (see Materials and Methods), any of the models available at the BioImage.IO model zoo (*12*) or Spotiflow (*2*). Detected structures are linked to individual cells using segmentation masks, enabling single-cell measurements. These are then used in conjunction with the intensity signal to compute several features from the reference channel, such as the reference channel structure volume, number of fragments, intensity-based features, etc. The binary masks of the spots channel are used to guide a 3D peak-detection pipeline that identifies peaks in the signal within the masks. The detected spots (peaks in the signal) are then quantified, and user-selected features can be used to filter valid spots. When false positive spots are removed, they become part of the background, hence requiring recalculation of features such as the SNR. To account for these changes, quantification and filtering are repeated until no more false positive spots are discarded. SpotMAX is available through a comprehensive, user-friendly graphical user interface (GUI) as a plugin for Cell-ACDC. Alternatively, it can be executed headless from the command line or embedded in custom pipelines through a high-level Python API.

option because part of the benchmarking dataset was used for training the U-Net models (see Materials and Methods). In fig. S3 instead, we compared Spotiflow fine-tuned on the same dataset to SpotMAX and tested on a test dataset that was not part of the training set. For the first category containing smFISH data, we also asked a junior scientist with no previous smFISH experience ("human" in Fig. 2B) to annotate the center of the spots (after an introduction about smFISH data). Since SpotMAX, Big-FISH, and RS-FISH require parameter selection, we selected a few random z-stack volumes and identified optimal parameters through visual inspection that resulted in the highest performance on this example dataset. We then ran the analysis on the entire dataset while keeping the same selected parameters for all tools. We found that on the smFISH dataset, SpotMAX outperformed the SOTA tools—while it is on-par with Piscis—and also the human annotator (Fig. 2B), a type of benchmark that none of the existing tools reported before (Friedman test: P value $= 5.78 \times 10^{-21}$; Wilcoxon two-sided signed-rank test, Holm-corrected P values and paired Cohen's effect sizes dz.: SpotMAX versus Big-FISH $P = 1.51 \times 10^{-10}$ and dz. = 1.77, SpotMAX versus U-FISH $P = 1.63 \times 10^{-7}$ and dz. = 1.87, SpotMAX versus Human

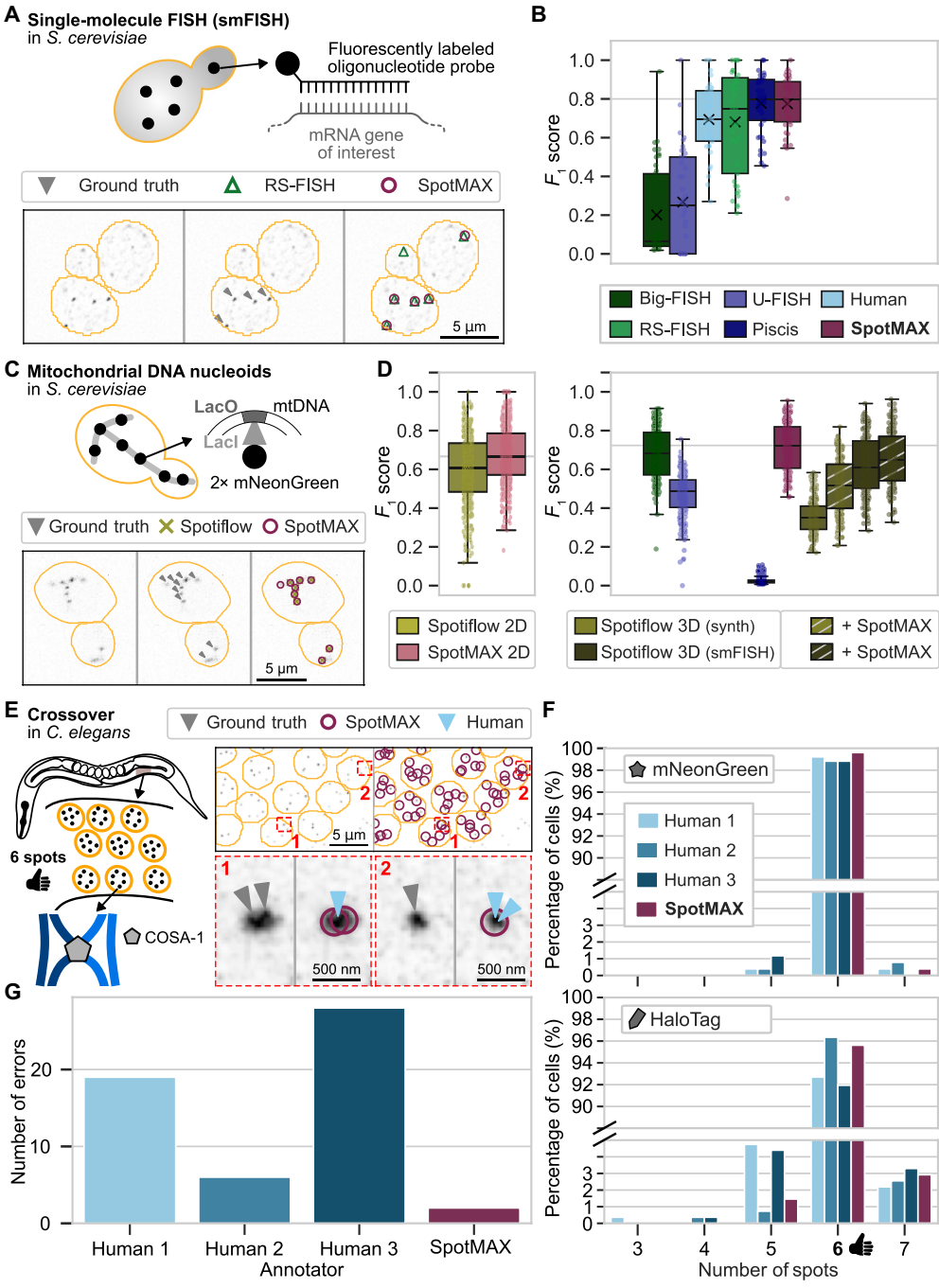

Fig. 2. Benchmark of SpotMAX in various experimental conditions. (**A**) Schematic of the first dataset: smFISH in *S. cerevisiae*, with representative images showing ground truth, RS-FISH (*1*), and SpotMAX annotations. Cell contours (orange) were obtained with Cell-ACDC. RS-FISH is shown as an example of false detection. (**B**) Benchmark results comparing Big-FISH (*3*), U-FISH (*9*), Human annotator, RS-FISH (*1*), Piscis (*7*), and SpotMAX. Ground truth was generated by an expert (373 cells, 41 z-stacks). The human annotator was a junior scientist trained by the expert. (**C**) Schematics of the second dataset: mtDNA nucleoids in *S. cerevisiae*, with representative images showing ground truth, Spotiflow (*2*), and SpotMAX annotations. (**D**) Benchmark results (357 cells, 190 z-stacks) comparing Big-FISH, U-FISH, Piscis, Spotiflow, and SpotMAX. Spotiflow pretrained models ("general," "synthetic," and "smFISH") were used. SpotMAX postprocessing ("+ SpotMAX") reduces false positives using multichannel features. (**E**) Schematics of the third dataset: COs in *C. elegans*, visualized via COSA-1 tagging. Ground truth is known (six crossovers per cell). Representative images show SpotMAX and human annotations, including counting errors. (**F** and **G**) Benchmark against three human annotators (548 cells, 3181 spots). Annotators differed in expertise and prior knowledge. While most counts were correct, variability was higher in the HaloTag dataset. SpotMAX achieved the lowest error rate (0.8%) and highest accuracy, with fewer errors than the expert annotators (Human 1: 19 errors, 3.4% error rate, $P = 0.9997$, $R = 0.9943$, $F_1 = 0.9970$; Human 2: 6 errors, 1.1% error rate, $P = 0.9997$, $R = 0.9984$, $F_1 = 0.9991$; Human 3: 28 errors, 5.1% error rate, $P = 0.9991$, $R = 0.9921$, $F_1 = 0.9955$; SpotMAX: 2 errors, 0.8% error rate, $P = 1.0000$, $R = 0.9994$, $F_1 = 0.9997$. P is precision, R is recall, and F_1 is F_1 score, while the "error rate" is calculated per cell). Details about the datasets used in this benchmark are available in table S1. Image intensities were adjusted for visualization purposes.

$P = 0.01$ and dz. = 0.45, SpotMAX versus RS-FISH $P = 0.03$ and dz. = 0.45, SpotMAX versus Piscis p = 0.83 and dz. = 0.01).

In the second category, the spots are mtDNA-protein complexes (nucleoids) that contain about one to three copies of mtDNA (*16*, *17*) and appear in the images as globular-like structures distributed along the mitochondrial network (Fig. 2C). Because the tools tested in the first category are all specific for smFISH data, for this second category, we included Spotiflow which was reported to outperform other SOTA tools on a different dataset (*2*). Because the most generalist version of Spotiflow can detect spots only in 2D images ("general" model), we first compared it to SpotMAX 2D and found that SpotMAX 2D had a higher F_1 score (Fig. 2D, left; Wilcoxon two-sided signed-rank test, Holm-corrected *P* values and paired Cohen's effect sizes dz.: SpotMAX 2D versus Spotiflow 2D $P < 1.00 \times 10^{-10}$ and dz. = 0.63). Next, we tested Big-FISH, U-FISH, Piscis, and the two available pretrained Spotiflow 3D models, "synthetic" and "smFISH", directly on 3D volumes. We found that SpotMAX 3D outperforms all tested tools (higher F_1 score for SpotMAX, Fig. 2D, right; Friedman test: *P* value $< 1.00 \times 10^{-10}$; Wilcoxon two-sided signed-rank test, Holm-corrected *P* values and paired Cohen's effect sizes dz.: SpotMAX versus Big-FISH $P = 1.20 \times 10^{-12}$ and dz. = 0.53, SpotMAX versus U-FISH $P < 1.00 \times 10^{-10}$ and dz. = 1.64, SpotMAX versus Piscis $P \leq 1.00 \times 10^{-10}$ and dz. = 5.01, SpotMAX versus Spotiflow 3D "synthetic" $P < 1.00 \times 10^{-10}$, and dz. = 3.28, SpotMAX versus Spotiflow 3D "smFISH" $P < 1.00 \times 10^{-10}$ and dz. = 1.00). However, we noticed that the lower Spotiflow performance was mainly due to higher false positives. Therefore, we reasoned that SpotMAX could be used to improve Spotiflow detections by using one of SpotMAX's features: the ability to leverage multichannel information to remove false positives (see Materials and Methods and fig. S4). By doing so, we show that SpotMAX improves the Spotiflow performance ("+ SpotMAX" in Fig. 2D, right), highlighting the power of a modular framework where any spot detection tool can be used as input for the subsequent analysis and refinement steps within SpotMAX. Still, even with the additional SpotMAX analysis, Spotiflow did not reach the F_1 score of SpotMAX 3D (Wilcoxon two-sided signed-rank test, Holm-corrected *P* values and paired Cohen's effect sizes dz.: SpotMAX versus Spotiflow 3D "synthetic" + SpotMAX $P < 1.00 \times 10^{-10}$ and dz. = 2.37 and SpotMAX versus Spotiflow 3D "smFISH" + SpotMAX $P < 1.00 \times 10^{-10}$ and dz. = 0.70). Next, we also fine-tuned both Spotiflow 3D and SpotMAX U-Net 3D on a training set from the Fig. 2 dataset. By benchmarking both models on the fraction of the mtDNA dataset unseen during training, we found that SpotMAX U-Net 3D had a higher median F_1 score than the fine-tuned Spotiflow 3D (fig. S3, Wilcoxon two-sided signed-rank test, Holm-corrected *P* values and paired Cohen's effect sizes dz.: SpotMAX 3D U-Net versus Spotiflow 3D fine-tuned $P = 0.06$ and dz. = 0.72). Last, we performed ablation experiments by progressively removing key components of the pipeline, first replacing the U-Net with automatic thresholding and subsequently disabling both the U-Net and preprocessing steps, resulting in a stepwise decrease in performance (fig. S5). Thus, SpotMAX consistently outperforms all other spot detection tools in this second category because it does not rely on a single approach but instead integrates AI-driven segmentation with classical signal processing methods.

In the third category, the ground truth for most of the objects is known a priori. Homologous chromosomes must form crossovers during meiosis to increase the genetic diversity of the gametes. This crossover formation is tightly regulated, and in *C. elegans*, each of the six pairs of homologous chromosomes typically receives exactly one crossover (*18*). Therefore, we observe six foci of the crossover marker COSA-1 in each nucleus after crossover designation (*19*) with cell-to-cell variation being rare (*20*). This dataset provides the opportunity to systematically compare SpotMAX to human annotators. For this purpose, we recruited three annotators with different backgrounds: (i) an expert of manual counting in smFISH datasets who did not know that six is the expected count per cell (Human 1), (ii) an expert with experience counting COSA-1 foci in *C. elegans* manually (Human 2), and (iii) a bioimage analysis expert who knew about the expected number of spots (Human 3). Counting spots in 3D is tedious, and spots are easily counted twice across neighboring z-slices. To minimize the occurrence of this type of error, we equipped Cell-ACDC with visual help where a spot is annotated on multiple neighboring z-slices. In addition, we stratified the counts over the fluorescent reporter used to visualize the COSA-1 foci: mNeonGreen and HaloTag, where mNeonGreen has a higher SNR than the HaloTag.

We found that the counts of COs in *C. elegans* differed between all three annotators and SpotMAX, with a high interannotator variability (Fig. 2, E to G). To count the number of errors, we carefully inspected the 77 cells where at least one of the annotators or SpotMAX did not agree on the count or on the location of the spots. Unexpectedly, we found that SpotMAX made only two errors, even less than the expert annotator of COSA-1 foci. The level of expertise with the specific dataset seems to matter because both Human 1 and Human 3 made considerably more errors. This demonstrates the importance of training annotators, a process that can take months, and highlights the value of automated image analysis with similar, or better, accuracy.

The process of crossover formation is tightly regulated, and small perturbations can have drastic effects. Any extra or missing crossovers can result in the mis-segregation of chromosomes during the meiotic divisions and produce aneuploid gametes that give rise to infertility or congenital conditions (*21*). Therefore, an unbiased, high-accuracy, and high-throughput method was desperately needed to measure these small perturbations.

Apoptosis targets meiotic nuclei with crossover errors, bypassing the DNA damage checkpoint

Automated and unbiased analysis is often key to answering open biological questions. For example, to study meiosis, understanding CO formation is fundamental because errors in this process are a major cause of infertility and can result in congenital conditions such as Down syndrome (*22*). A widely used model organism in this field is *C. elegans*. Most of the cells in the germ line of this animal form six COs. In wild-type animals, very few cells will have an abnormal number of COs (Fig. 3, A and B). To ensure the genetic integrity of the offspring, most of these nuclei should be promptly removed by apoptosis. However, exactly how this process works and how apoptosis is triggered under these circumstances are unknown. To investigate the rare occurrence of an aberrant number of COs in *C. elegans*, manual counting, while widely used and effective due to its low error rate, lacks the throughput necessary to study these infrequent events.

Therefore, we tested SpotMAX's ability to accurately count spots in a large number of cells in a fully automatic and unbiased way. To visualize the COs, we first generated two *C. elegans* strains carrying the endogenous reporters HaloTag and mNeonGreen fused to the COSA-1 gene, a key component of CO formation (*19*). More details about the dataset are available in table S2.

Next, we used SpotMAX to compare the robustness of different markers for COSA-1 by quantifying the native fluorescence of three

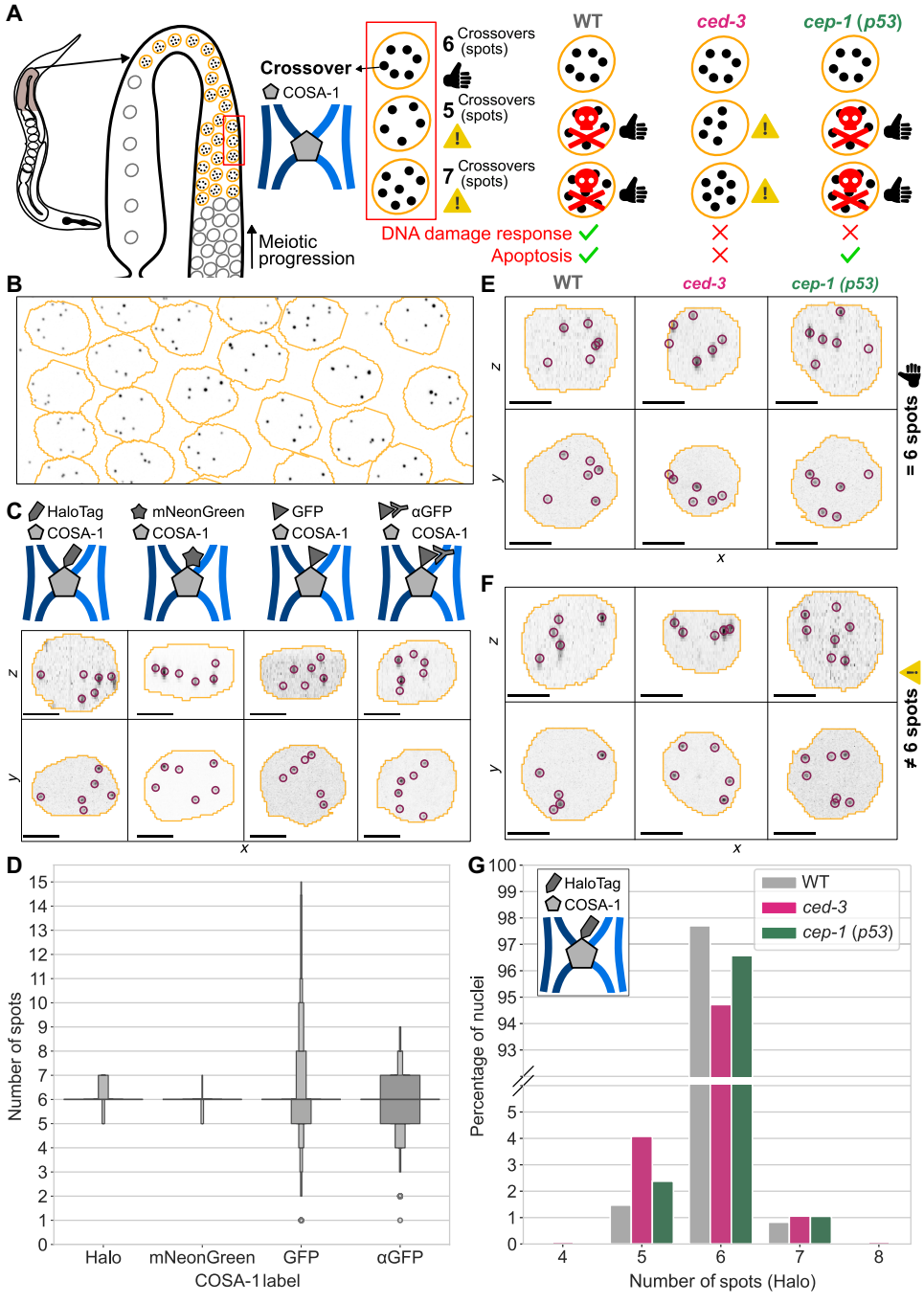

Fig. 3. SpotMAX analysis of the crossover error regulation process in *C. elegans*. (**A**) Schematic representation of the experimental setup and conditions in mutant strains. The expected number of COs in wild-type cells is six. In a small number of cells, five or seven COs might form. By deleting *ced-3*, apoptosis is inhibited, resulting in more cells with an abnormal number of COs. By deleting *cep-1* (*p53*), only the DNA-damage response-triggered apoptosis is inhibited, but the cells with abnormal numbers of COs are still removed. (**B**) Representative image of cells within the germ line from the COSA-1::mNeonGreen strain (see C). (**C**) Schematic representation of the four methods we tested to visualize COs, and representative images for each method with SpotMAX annotations (purple circles) and segmentation outlines generated with Cell-ACDC (*58*). GFP, HaloTag, and mNeonGreen are fluorescent proteins fused to COSA-1, while αGFP refers to antibody staining of the GFP (gold standard). (**D**) Letter-value plots (*61*) showing the number of COSA-1 spots (Number of Spots) quantified with SpotMAX for the four visualization methods (see C). Number of nuclei: Halo = 453, mNeonGreen = 603, GFP = 630, αGFP = 630. (**E**) Representative images of wild-type (wt), *ced-3*, and *cep-1* (*p53*) deletion mutants, where the number of COs is the expected value of 6. Purple circles are the SpotMAX detections, while the orange outlines are the segmentation masks generated with Cell-ACDC. (**F**) Same as in (E), but for cells that have more or less than six spots. (**G**) Histograms of the number of COs in cells without unrepaired DNA damage (number of spots) counted with SpotMAX in WT, *ced-3*, and *cep-1* mutants (Halo::COSA-1 staining). Number of nuclei: wild type (WT) = 1698, *ced-3* = 1325, and *cep-1* = 1430. Scale bar, 2 μm. Image intensities were adjusted for visualization purposes.

reporters [green fluorescent protein (GFP), mNeonGreen, and HaloTag] (Fig. 3C) and antibody staining of the GFP reporter. The GFP::COSA-1 reporter is expressed from an integrated multicopy transgene. Halo::COSA-1 and COSA-1::mNeonGreen are endogenously tagged by CRISPR/Cas9 mediated genome editing (see Materials and Methods) and are fully functional (table S4). mNeonGreen surpasses the commonly used GFP::COSA-1 reporter in brightness and SNR, while the spot intensities of Halo::COSA-1 are the least variable (fig. S6A) (Fig. 3D). By contrast, the antibody staining of GFP::COSA-1 introduces a surplus of nuclei with more than six foci due to an increase in background staining resulting in a lower SNR.

The fact that 97% of meiotic cells designate exactly one crossover on each of the six pairs of homologs, resulting in six spots per nucleus, highlights the robustness of the regulatory mechanisms controlling crossover number and distribution during meiosis. Alternatively, or in addition, there may be a checkpoint that eliminates nuclei with an incorrect number of crossovers. Cells (50%) are removed through apoptosis during meiotic prophase in *C. elegans* (*19*), and persistent defects in the meiotic program can activate apoptosis of meiotic cells across metazoans (*22*). We wondered if nuclei with abnormal numbers of designated crossovers are preferentially targeted for apoptosis to enhance the robustness of crossover regulation. Therefore, we compared the percentage of nuclei with aberrant numbers of Halo::COSA-1 foci in wild-type and *ced-3* animals (Fig. 3, A, E, and F), which cannot initiate programmed cell death in both somatic and germline cells (*23*). In wild-type animals, only 2.7% of nuclei had aberrant numbers of COSA-1 foci compared to 6.5% in *ced-3* animals (fig. S6B). Most nuclei with aberrant COSA-1 foci had five or fewer foci, suggesting some chromosomes lacked a crossover. Crossover assurance promotes double-strand break formation until each chromosome pair has at least one crossover (*24*). The absence of a crossover on some chromosomes might result from incomplete repair of breaks into crossover precursors, which should trigger apoptosis via the DNA damage checkpoint. We tested whether *cep-1* (*p53*) knockout animals, which are deficient in DNA damage–induced apoptosis (*25*, *26*), exhibited similar aberrant COSA-1 foci numbers as *ced-3* animals. *cep-1 (p53)* animals had 4.1% of nuclei with aberrant COSA-1 foci, lower than *ced-3* animals but slightly higher than wild-type animals (fig. S6B).

This finding suggests that nuclei with aberrant numbers of designated crossovers are targeted for apoptosis both through activation of the DNA damage checkpoint and independently of it. To test this hypothesis, we quantified spot numbers selectively in nuclei that did not have any markers of residual DNA damage. Specifically, using SpotMAX, we identified nuclei with remaining unrepaired breaks (*27*), visualized by staining for V5::RAD-51, and excluded these nuclei from our analysis. In this refined analysis, *cep-1 (p53)* animals displayed similar numbers of COSA-1 foci per nucleus as wild-type animals [wild-type: 97.3% nuclei with six spots (5.99 ± 0.14 spots), *cep-1 (p53)*: 95.9% nuclei with six spots (5.99 ± 0.18 spots); two-sided Student's *t* test *P* value of WT-vs-*cep-1* = 0.298]. However, *ced-3* animals still had significantly fewer nuclei with six COSA-1 foci [94.7% (5.97 ± 0.24 spots), two-sided Student's *t* test *P* value of WT-vs-*ced-3* = 0.0015] (Fig. 3G). Thus, the high-throughput automated analysis of thousands of nuclei enabled by SpotMAX revealed an unexpected mechanism that selectively targets nuclei with errors in crossover regulation for apoptosis independently of the DNA damage checkpoint.

Asymmetric inheritance promotes fast adaptation of mtDNA copy number in *S. cerevisiae* daughter cells

So far, we tested SpotMAX's ability to use the 3D information of z-stack volumes in a single fluorescence microscopy channel. However, many microscopy datasets are 5D, including multiple channels, such as bright field or phase contrast for tracking single cells, additional fluorescence channels (e.g., organelles), and a time dimension. Therefore, we reasoned that using information from these additional dimensions and channels could improve the overall accuracy and provide new biological insights. With time-lapse microscopy data, crucial information comes from cell identity and cross-generational pedigree information. SpotMAX is integrated into the Cell-ACDC (*11*) framework, which provides access to segmentation, tracking, and cell-pedigree annotation in a format that is fully usable by SpotMAX. In addition, to test SpotMAX's capabilities to accurately quantify subcellular structures in 4D microscopy time-lapse data, we asked whether it could be used to reveal the dynamic adaptation of budding yeast mitochondria to a nutrient shift. Budding yeast can adopt two different types of metabolism, respiration, and fermentation, and it up-regulates the copy number of its mtDNA and the mitochondrial network volume when it respires (*16*, *28*). Yeast cells mainly perform respiration, requiring mtDNA, when provided with galactose as the sole carbon source (*29*). We thus expect a higher mtDNA copy number and mitochondrial network volume than in cells growing on glucose media, where they can rely on anaerobic fermentation independent of mtDNA. To follow the dynamics of this adaptation, we imaged live budding yeast single cells for over 7 hours going through a medium change, from respiratory medium (SCGal, 2% galactose) to fermentation medium (SCD, 2% glucose). To visualize the mitochondrial network and mtDNA, we used a previously established system based on LacO arrays stably integrated into the mitochondrial genome and endogenously expressed fluorescent reporter proteins (see strain FPY004 in table S3) (*16*, *30*). This system allows us to visualize the mitochondrial network (green in Fig. 4, A and B) and the mtDNA (magenta in Fig. 4, A and B; spot detections in orange circles). More details about the dataset are available in table 2. After data acquisition, we segmented and tracked the cells, annotated the cell cycle progression, and calculated the cell volume from the bright-field channel using Cell-ACDC (*11*). The tracked segmentation masks were used as input for SpotMAX, which automatically segmented the mitochondrial network, quantified its volume, and counted the number of spots in each cell at every time point. Using the cell division annotation, we followed the evolution of the mitochondrial network volume and the nucleoid number at a given cell cycle stage (Fig. 4, C and D). We found that, directly after cell division, the density of mitochondria network volume and nucleoids decreased in both mother and daughter cells after shifting from the respiratory medium to the fermentation medium. However, the concentration in the daughter cells decreases faster than in the mother cells. This differential regulation in mother and daughter cells was observed at the first time point after cell division. Since other types of regulation such as mitophagy are unlikely to happen on this short time scale (15 min), our findings suggest that yeast achieves a rapid adaptation of daughter cells to the new nutrient condition through asymmetric inheritance of the mitochondria and mtDNA.

Telomere length is unchanged in large HSCs

In many applications, spot counting is not enough, and we need to quantify the intensities of the spots. To achieve this, we equipped

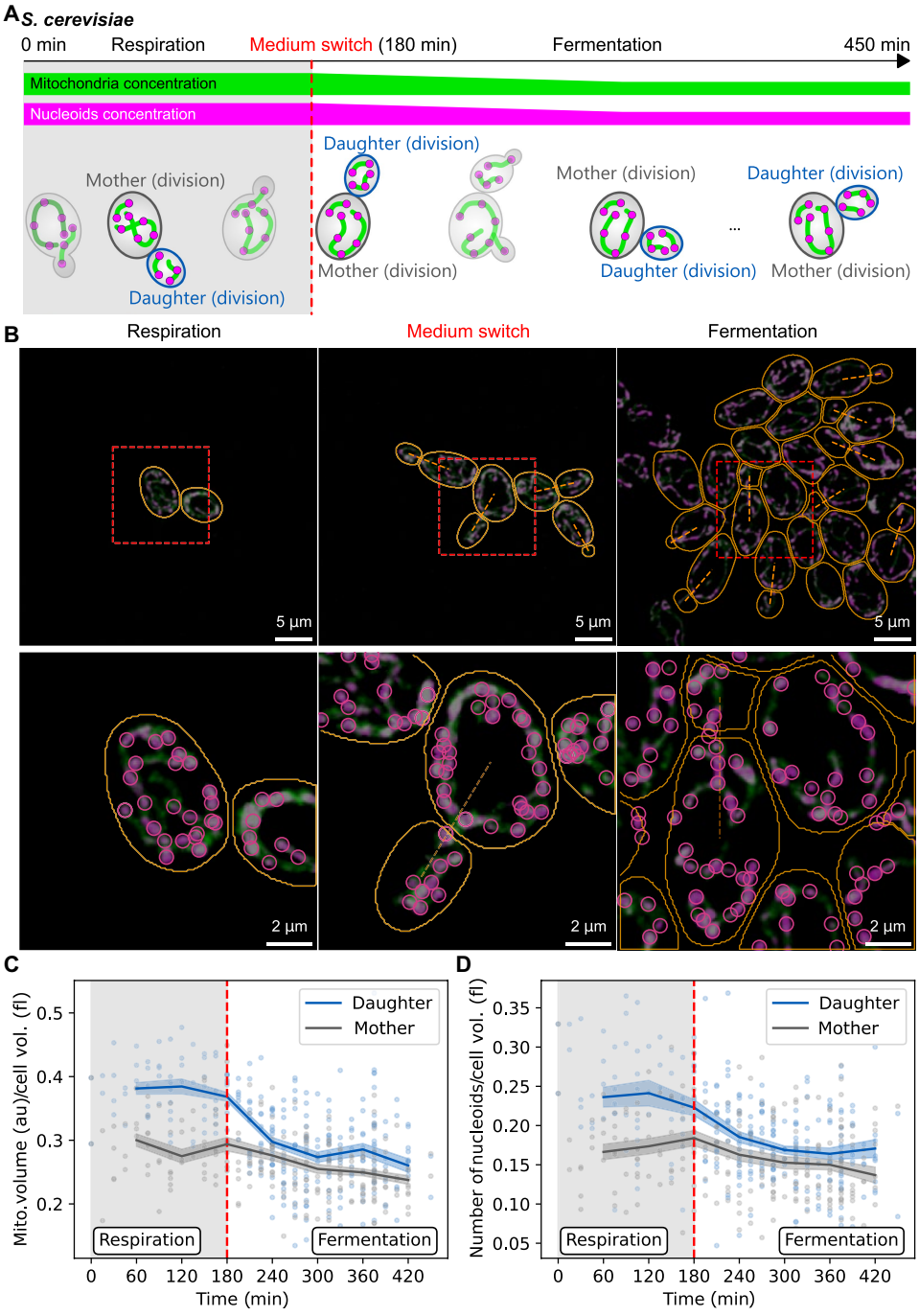

Fig. 4. Mitochondria and nucleoid concentration in live *Saccharomyces cerevisiae* cells during a nutrient shift. (**A**) Schematic representation of the experimental conditions. To assess SpotMAX on dual-channel time-lapse data, *S. cerevisiae* cells were imaged during a metabolic shift from respiratory to fermentative conditions, a transition known to lower concentration of mtDNA, nucleoids, and mitochondria content. After segmenting, tracking, and annotating mother-daughter relationships with Cell-ACDC, we computed the mitochondrial network volume from the reference channel and the number of nucleoids (spots), each directly after the time of division for mother cells and their daughters. We used the same visualization approach as depicted in Fig. 2C. (**B**) Representative images of budding yeast cells with mitochondrial network (green) and nucleoids (magenta) channel from three time points: start of the experiment (respiration), medium switch, and end of the experiment (fermentation). The orange outlines show the segmentation masks, while the orange dashed lines show the mother-daughter relationships. The zoomed images show the SpotMAX annotations (pink circles) of the cells present in the first frame and their relative daughters. Note that the magenta spots that appear not detected are those spots that did not pass quality control, including the comparison to the reference mitochondrial network channel (fig. S4). (**C**) Mitochondrial network volume and (**D**) the number of nucleoids divided by cell volume (concentration) for the cells at division as a function of time since the start of the experiment. Note that we plotted only those cells that were present at the medium switch (red dotted line). Points show data corresponding to individual cells. The line represents the mean, and the shaded area is the 95% confidence interval of the mean calculated by bootstrapping (1000 bootstrap resamples). Details about the dataset size are available in table S2. Image intensities were adjusted for visualization purposes.

SpotMAX with the SpotFIT module, which provides the ability to quantify the total fluorescence intensity of each spot (see Materials and Methods). To test this functionality in a biological application, we focused on the relationship between telomere length and cell size. The declining function of HSCs during aging is associated with an increase in their cell size (*31*), but how cell size affects HSC functionality is unknown. One potential explanation is telomere shortening, which is linked to cellular aging and causes senescence and apoptosis of somatic cells (*32*, *33*). However, whether this also applies to HSCs is still unclear (*34*). For example, during division of HSCs, telomeres become shorter (*35*). Nevertheless, preventing this shortening by telomerase overexpression does not prevent HSC exhaustion in mice (*34*). To further evaluate the role of telomere shortening in HSC aging, we analyzed telomere length in small, medium, and large HSCs using DNA-FISH against telomeric repeats. Next, we used SpotMAX to detect telomeres and calculated integrated spot intensities since they correlate with telomere length (*36*) (Fig. 5, A and B). As a control for which we did not expect changes in spot intensities, we stained centromeres. We used Cell-ACDC to segment HSCs and then automatically quantified telomere and centromere spot numbers and spot intensities using SpotMAX. More details about the dataset are available in table S2.

SpotMAX detected 18 centromeric spots of variable brightness (on average, purple in Fig. 5C) in line with previously reported values (*37*). The high variability is likely due to centromere clustering, but the number of centromeric spots stayed constant with increasing cell size (Fig. 5C and fig. S7A), suggesting that cell size does not affect their detection. Similarly, the number of detected telomere spots was unchanged in larger HSCs. Next, we investigated the mean total intensity of the telomere and centromere spots (Fig. 5D and fig. S7B). We observed that telomere length did not change strongly in enlarged HSCs, suggesting that their dysfunction is not caused by telomere shortening (Fig. 5D). Overall, these results demonstrate that SpotMAX enables the reliable and efficient detection and analysis of

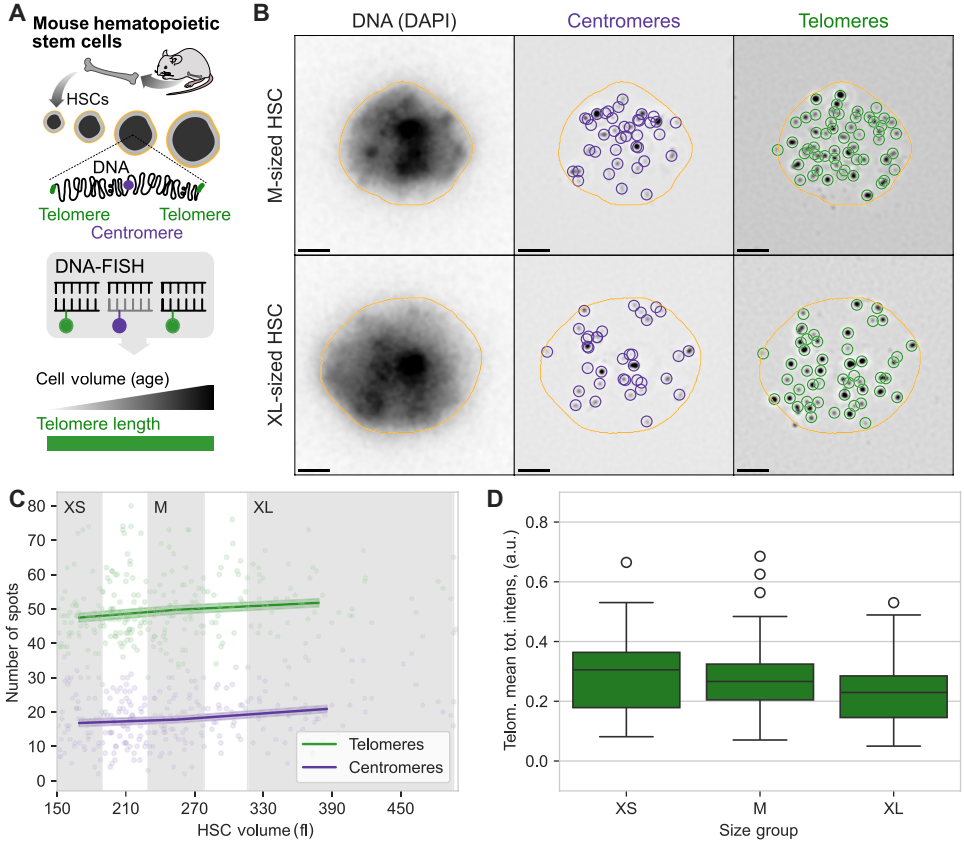

Fig. 5. Telomeres and centromeres visualized with DNA-FISH in HSCs. (**A**) Schematics of the experimental protocol. After extracting HSCs from mice bone marrow (see an example of gating strategy in fig. S8), we visualized the centromeres and telomeres with DNA-FISH. (**B**) Representative images of medium-sized (M) and extra-large (XL) HSCs from wild-type mice showing DNA [4′,6-diamidino-2-phenylindole (DAPI)], the telomere (Cy3, purple circles), and centromere (Alexa488, green circles) DNA-FISH signal. Circles indicate the SpotMAX detections, and the orange outlines show the cell segmentation masks obtained with Cell-ACDC (*11*). (**C**) Number of spots as a function of HSC volume (fl) for telomeres and centromeres. Gates of XS-, M-, and XL-sized HSCs are indicated in gray. Cells with a volume less than 130 fl were discarded from the analysis because the number of spots was variable with cell size, indicating a detection limit in smaller cells. The full analysis is shown in fig. S7A. Points in the plot represent single-cell data, the line shows the mean and the shaded area is the 95% confidence interval of the mean calculated with 1000 bootstrap resamples. (**D**) Mean total intensity of the spots in the single cells for each size category. Number of cells per category: XS = 54, M = 65, XL = 54, total = 173. The difference between the groups is not statistically significant (two-sided Student's *t* test, Bonferroni adjusted *P* values: XL-vs-XS = 0.186, M-vs-XS = 0.697, and M-vs-XL = 0.186). The total intensity (column name foreground_integral_fit) was calculated by integrating the Gaussian curve fitted to the data in the SpotFIT step of the SpotMAX analysis. The total intensity of the spots in each single cell was then averaged to obtain the mean total intensity. The length of the scale bar is 2 μm. Image intensities were adjusted for visualization purposes. a.u., arbitrary unit.

fluorescence spots of murine stem cells. Furthermore, our data suggest that telomere length is not a major contributor to the cellular aging of enlarged HSCs.

Nucleolus and nuclear size decrease upon DAF-15 (Raptor) depletion in the *C. elegans* intestine

Next, we asked whether SpotMAX can be used to quantify the volume of larger cellular structures in 3D microscopy data of a complex, multitissue organism. Specifically, we decided to test the quantification of the nucleolus and again chose *C. elegans* as a model. Nucleolar size typically reflects the activity of ribosome biogenesis (*38*, *39*). Nucleolar size is regulated by the mechanistic target of the rapamycin (mTOR) signaling pathway (*40*, *41*). mTOR is a master regulator of ribosome production, particularly through the mTOR complex 1 (mTORC1), which regulates cell growth in response to nutrients (*42*). Thus, to test the ability of SpotMAX to quantify changes in nucleolar volume, we used animals expressing the nucleolar marker FIB-1::mCherry (Fibrillarin) (*40*) and HIS-72::GFP (H3.3) to label nuclei. We used the auxin-inducible degradation system (*43*) to degrade DAF-15, the *C. elegans* homolog of mammalian Raptor, a specific component of mTORC1 (*44*). More details about the dataset are available in table S2. We imaged larvae treated with auxin or ethanol as a control, segmented intestinal nuclei with Cell-ACDC (*11*) using the HIS-72::GFP (H3.3) signal at the central z-slice of each nucleus and used the masks to estimate the 3D volume from the 2D masks, as explained in (*45*). To validate the 3D volume estimation, we performed stratified sampling and selected 40 of the 357 nuclei for 3D segmentation. Specifically, nuclei were binned into quantiles of the volume (estimated from 2D masks) distribution (20 bins) and sampled proportionally from each bin. This ensured that the sampled subset preserved the full dynamic range and distribution of the population, as confirmed by overlapping density histograms (fig. S9A) and a low Kolmogorov-Smirnov statistic (KS statistic = 0.042, *P* value = 1.0). Next, we computed the volume from 3D segmentation masks and plotted it against the volume estimated from 2D (fig. S9B). We observed a strong agreement between volume calculated from 2D and from 3D masks, indicating that the volume from 2D is quantitatively accurate and monotonic across the entire distribution (Spearman coefficient = 0.850, *P* value $\leq 10^{-10}$; Pearson coefficient = 0.851, *P* value $\leq 10^{-10}$). The nuclei masks were then used as input for SpotMAX (which automatically expanded the 2D segmentation masks 10 z-slices above and below the segmented one) to detect and quantify the volume of the corresponding nucleoli in 3D (Fig. 6, A and B). Consistent with previous studies that directly perturbed the LET-363 (mTOR) kinase (*40*, *41*), we found that the depletion of DAF-15 markedly decreases nucleolar volume (Fig. 6C).

While the impact of mTOR on nucleolar size is well documented in different biological systems (*38*, *40*, *46*), it is less clear whether it also affects nuclear size. Using the segmentation masks described above, we quantified the HIS-72/H3.3-GFP signal as a readout for nuclear size and found that the volume of intestinal nuclei is also reduced upon DAF-15 degradation (Fig. 6C). However, the relative reduction in size is greater for the nucleolus compared to the nucleus, revealing that intestinal cells of mTORC1-inhibited animals have a reduced nucleolus-to-nucleus volume ratio.

DISCUSSION

Here, we presented SpotMAX, a generalist 3D spot detection and quantification tool for the analysis of fluorescence microscopy data. SpotMAX introduces several innovations: (i) it detects spots in 3D and can leverage multidimensional information, including multiple fluorescence channels and time information; (ii) it goes beyond spot detection by computing biologically meaningful features, which can also be used to identify true spots; (iii) it provides a glue framework for any existing or future spot detection models; (iv) it outperforms expert human annotators; and (v) it is generalist, versatile, and application-independent. By integrating information from z-stacks, multiple channels, and segmentation masks with tracked cells over time, SpotMAX enables more reliable identification of true biological foci, reduces false positives arising from noise, and computes biologically relevant features. Along with SpotMAX, we also publish a high-quality, manually annotated, 3D ground truth dataset of experimental data from various experimental protocols and imaging modalities composed of 369 z-stack volumes with 20,692 annotated spots from 2894 cells. This dataset is the first public dataset of its kind, and it can therefore serve as a reference to test or train future spot detection tools. We showed that SpotMAX outperforms current SOTA tools and can provide new biological insights, a result made possible by several improvements compared to existing tools. First, SpotMAX uses both AI-based and traditional computer vision algorithms, including a custom-made 3D U-Net architecture and existing AI tools such as Spotiflow and any of the models available on the BioImage.IO zoo (*12*). Paired with a user-friendly GUI and tight integration with Cell-ACDC (*11*) and other existing tools, we provide a framework for experimental biologists to tackle open biological questions without advanced technical knowledge of complex bioimage analysis pipelines. Second, SpotMAX goes beyond spot detection by computing several morphological and intensity-based features that allowed us to achieve a substantial performance increase. This markedly simplifies the building of image analysis pipelines where spot counting is not enough.

Last, to meet the current demands of running workflows on high-performance computing (HPC) environments, we provide both the possibility to run SpotMAX headless from the command line as well as from Python Application Programming Interface (API). We also provide extensive documentation, including comprehensive written and video tutorials. This headless operation can be especially valuable to software developers and bioimage analysts who need to integrate spot detection and quantification algorithms within existing workflows. Furthermore, the analysis of multiple images can be readily parallelized in HPC environments.

We believe that SpotMAX's ability to go beyond SOTA spot detection with a framework for accurate multichannel and multidimensional quantification and its tight integration with other AI pipelines will make it a reference software for experimental biologists addressing spot quantification tasks.

MATERIALS AND METHODS

SpotMAX is written in Python v3 and published on the Python Package Index repository. We extensively documented SpotMAX, including two tutorials with experimental data. The documentation can be found at https://spotmax.readthedocs.io/en/latest/index.html and the source code is hosted on GitHub at https://github.com/SchmollerLab/SpotMAX. Video tutorials can be found at www.youtube.com/@cellacdc. SpotMAX can be used as a plugin of Cell-ACDC (*11*, *47*), which is a user-friendly GUI written with QtPy and PyQtGraph.

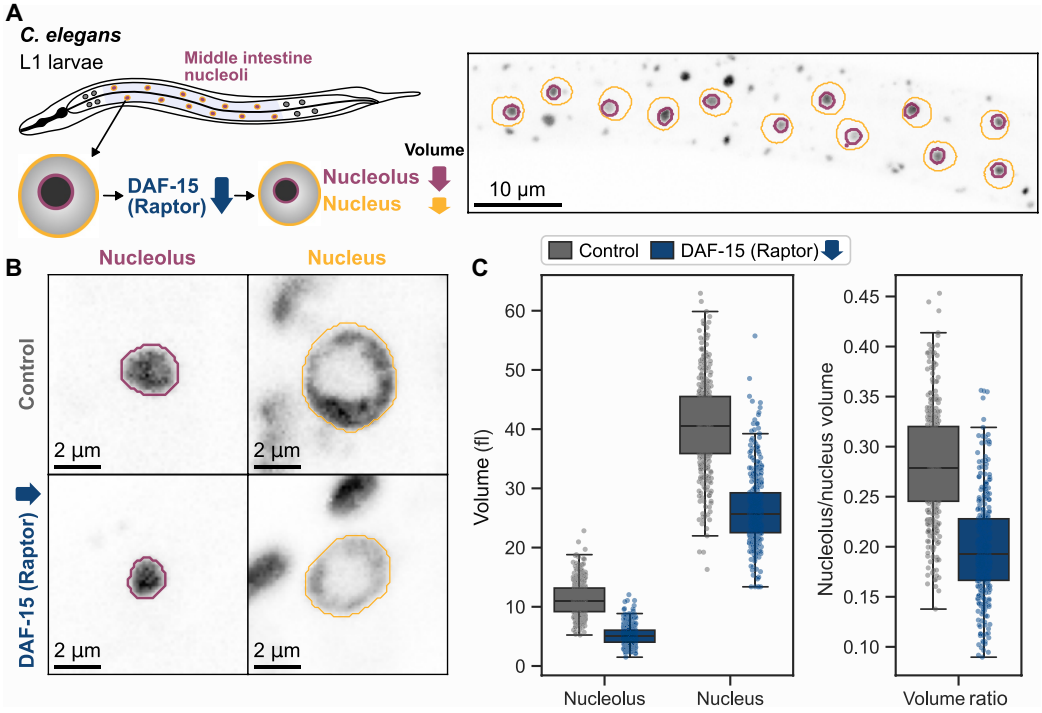

Fig. 6. Nucleolus and nucleus size upon DAF-15 (Raptor) depletion in the *C. elegans* intestine. (**A**) Schematic representation of the experimental protocol. To test SpotMAX's capabilities to segment globular structures and compute their volume, we quantified the nucleolus and nucleus volume decrease upon DAF-15 (Raptor) depletion in the 12 middle intestine cells of *C. elegans* L1 larvae. The representative image on the left shows the 12 intestinal nuclei segmented with Cell-ACDC (orange outlines) in the nucleoli channel. Purple outlines represent SpotMAX's automatic segmentation of the nucleoli (spots). (**B**) Representative images of the nucleolus (purple outlines, calculated by SpotMAX) and the nucleus (orange outlines from Cell-ACDC) channels in both the control and DAF-15 depleted strains. (**C**) Volume of the nucleolus, the nucleus and the nucleolus/nucleus ratio in the control ($n = 357$) and DAF-15 ($n = 358$) depleted strains. Two-sided Student's t test P values WT-vs-DAF-15 for nucleolus, nucleus, and volume ratio are all $<10^{-10}$. Details about the dataset size are available in table S2. Image intensities were adjusted for visualization purposes.

Alternatively, it can be deployed in a high-performance computing environment from the command line or with the Python API.

Modular architecture

As mentioned above, one of the most user-friendly ways to use SpotMAX is through Cell-ACDC. Cell-ACDC is automatically installed by SpotMAX when launching the tool for the first time, and it provides several modules to go from raw microscopy files to fully segmented, tracked, and annotated data. Once installed, SpotMAX can be launched from the Cell-ACDC launcher as any of the other Cell-ACDC modules. The SpotMAX GUI provides several advantages: (i) interactive fine-tuning of the parameters through automatic routines and/or visualization of intermediate results, such as visualization of the output of preprocessing filters and all segmentation methods available, including the SpotMAX AI model; and (ii) visualization and inspection of the results, including the location of the detected spots on the image and numeric indicators to inspect specific feature values.

To ensure full integration with existing and complementary tools, the input for the intermediate steps of the analysis can also be provided from external software tools. These inputs are provided as file paths pointing to the file with the results to be used. The inputs to the intermediate steps that can be provided externally are the following: (i) segmentation masks of the objects containing spots (e.g., single cells; typically from Cell-ACDC), (ii) spots channel segmentation masks, (iii) reference channel segmentation masks, (iv) spots coordinates table, and (v) table with cell pedigree and lineage information. The file formats supported for inputs 1 to 3 are .tif, .npy, .npz, and .h5. The file formats supported for inputs 4 and 5 are .csv, and .h5. For example, the user could already have a pipeline to segment the cells with Cellpose (*48*) for input 1, spot segmentation with ilastik (*49*) for input 2, nuclear segmentation with Stardist (*50*) for input 3, and spot detection with Big-FISH (*3*) for input 4, and then use SpotMAX for the feature extraction, quantification, and further filtering for true positives. Last, we provide high-level Python APIs with a single function for each of the intermediate steps, allowing users to easily build custom pipelines.

Robustness across imaging modalities

To ensure that SpotMAX generalizes across diverse imaging conditions and modalities, we designed the pipeline to minimize dependence on absolute intensity values and to adapt to varying signal characteristics. First, spot detection can be performed using either automatic thresholding, a trainable U-Net model (see below), or any of the models available at BioImage.IO model zoo, enabling the method to adapt flexibly to datasets with varying SNRs and imaging properties. Second, downstream feature extraction relies on intensity-normalized statistics that are largely independent of absolute signal levels. In particular, true positives are identified using effect size metrics and statistical tests (e.g., P values). We found effect size to be especially effective, because it provides values that fall in the same range across image modalities. To

account for cell-to-cell variability, SpotMAX can use the provided single-cell segmentation masks to normalize effect sizes by the per-cell background standard deviation, which improves the robustness of effect size metric as an efficient filtering criterion. Last, SpotMAX incorporates multiple preprocessing strategies designed specifically for spot-like structures or to fit different reference channel structures. A difference-of-Gaussians filter enhances spot-like features using the user-defined expected spot size, thereby improving detection sensitivity. In addition, Gaussian smoothing is used to reduce high-frequency noise, while a Sato filter can be applied to enhance network-like structures (e.g., the mitochondrial network) when relevant.

SpotMAX AI architecture and training

The SpotMAX AI model comprises 2D and 3D models with a U-Net-style architecture written with PyTorch (*51*). The 2D model is custom-made, while the 3D model is based on the library pytorch-3dunet (*52*).

Models

The 2D and 3D model architectures are shown in fig. S1. Both models use an encoder-decoder architecture with a sequence of batch normalization, convolution layers, Rectified Linear Unit (ReLU), and max pooling. In addition, each feature map of the encoder is concatenated to its corresponding feature map of the decoder. The final step consists of a convolution layer with a 1×1 kernel size to obtain the two classes, the background and the foreground. A pixel in the foreground is a pixel predicted as belonging to a spot (i.e., semantic segmentation).

Datasets and ground truth generation

The ground truth data for the training of the SpotMAX AI models consists of binary masks of the spot signal of various datasets. Specifically, we used previously published 3D datasets analyzed with Cell-ACDC (*14*–*16*) (for both 3D and 2D models) and the 2D "smfish" and "sun-tag" datasets used in the deepBlink software (for the 2D model) (*6*). To generate the spot masks, we started from the (x, y, z) spot coordinates provided by the corresponding publications, and we generated binary masks by placing a spheroid with fixed radii (different z radius to accommodate anisotropic volumes) in each spot center. The radii were calculated using the Abbe diffraction limit formula in x and y and multiplied by 3 to obtain the radius in z. These masks were manually inspected and, if necessary, corrected by an independent expert annotator using the Cell-ACDC software. The dataset was then split into train, validation, and test sets. The final dataset is composed of 4956 training z-slices, 1471 validation z-slices, and 1586 test z-slices.

Image preprocessing

Before feeding the model, the images are preprocessed in three steps: (i) resizing based on the pixel size to match a final pixel size of 73 nm/pixel; (ii) grayscale morphological opening to remove hot pixels artifacts (isolated bright pixels); and (iii) MinMax scaler, which scales each image to the (−1, 1) range based on the global minimum and maximum in each dataset.

Training

Both models were trained using stochastic gradient descent. The 2D model was trained for 100 epochs with a batch size of 16 images cropped to 400×400 size. Since the information in the z direction is not encoded by the model, z-slices were randomly shuffled before entering the model. For the loss function, we used the inverse of the Dice score. For the learning rate, we used a scheduler that, starting from a value of 0.001, reduces the rate after the validation score stops improving for more than eight epochs. As a result, the learning rate started decreasing around the 25th epoch and reached a final value of 1×10^{-8}.

For the 3D model, we divided the datasets into patches to reduce the computational cost, which can be high when working with 3D convolutional layers. The patches were extracted using a (z, y, x) patch size of (30, 250, 250) pixels with a stride of (20, 100, 100). Note that we tested several patch and stride sizes and selected the ones that resulted in the best performance. Furthermore, unlike with the 2D model, z-slices were not shuffled, since the correct order is important for the 3D operations. Last, we used a batch size of 4 and 15,000 training steps with the same learning rate scheduler used for training the 2D model.

All training runs were performed on a GPU Nvidia Tesla V100 with 32 gigabytes on the de.NBI Cloud within the German Network for Bioinformatics Infrastructure [funded by Federal Ministry of Education and Research (BMBF)]. The training time for a single run was around 5 hours for the 2D model and 8 hours for the 3D model.

3D Gaussian fitting procedure (SpotFIT)

To quantify spots with an intensity profile similar to a normal distribution, SpotMAX fits 3D Gaussian functions to the spots' signal. The 3D Gaussian function is defined as follows

$$g(x,y,z) = g(x)\, g(y)\, g(z) + B \tag{1}$$

where B is a fitting parameter and $g(x)$, $g(y)$, and $g(z)$ are 1D Gaussian functions given by

$$g(x) = A \exp\left(-\frac{(x - x_c)^2}{2\sigma_x^2} \right) \tag{2}$$

where x_c, σ_x, and A are fitting parameters for the spot center coordinate, the width, and the amplitude of the Gaussian peak, respectively. The integrated spot intensity used in the telomere length analysis in HSCs is calculated as follows

$$A\, s_x\, s_y\, s_z\, d_{\mathrm{erf}}(x)\, d_{\mathrm{erf}}(y)\, d_{\mathrm{erf}}(z) \tag{3}$$

where $s_x = \sqrt{\pi/2}\, \sigma_x$ and the same for the other dimensions and $d_{\mathrm{erf}}(x)$ is defined as follows

$$d_{\mathrm{erf}}(x) = \mathrm{erf}\left(\frac{x_1}{\sqrt{2}\, \sigma_x} \right) - \mathrm{erf}\left(\frac{x_0}{\sqrt{2}\, \sigma_x} \right) \tag{4}$$

with erf being the error function. x_1 and x_0 are the upper and lower bounds coordinates around the peak center, and they are $x_1 = 1.96\, \sigma_x$ and $x_0 = -1.96\, \sigma_x$. The same is then calculated for the y and the z directions. Note that the integrated spot intensity automatically excludes the background because it does not include the fitting parameter B. This metric is also referred to as "Foregr. integral gauss. peak" in SpotMAX documentation (column name "foreground_integral_fit").

Since fitting all pixels in the image is computationally infeasible and spots are often close to each other, we designed a workflow to determine relevant pixels. To account for differences in spot sizes, SpotMAX identifies the relevant pixels for each spot by iteratively enlarging the spheroid footprints by one pixel in each direction until the mean of the outer pixels in the spheroid mask falls below a threshold. This threshold is calculated as the background median plus three times the background standard deviation. Next, during the SpotFIT routine, SpotMAX fits one or more 3D Gaussian peaks to the spot intensities in the previously determined spot masks. To achieve the highest accuracy possible, with N touching spots, the sum of N Gaussian peaks should be fitted. However, this becomes extremely

computationally intensive with an increasing number of touching spots. Therefore, we implemented a computationally efficient procedure where the number of Gaussian peaks fitted is minimized. Given a group of touching spots, SpotMAX sorts the spots based on the number of direct neighbors in ascending order and starts from the spot that touches the least number of spots and runs the fitting procedure with this spot and its direct neighbors.

For every fitting step, only the current spot with its direct neighbors is fitted. The indirect neighbors are instead added to the model with initialized parameters that are not fitted. Indirect neighbors' parameter initialization is performed with an initial guess or with parameters from the previous iteration (when the indirect neighbor was a spot being fitted). After fitting the current spot, SpotMAX moves to the next spot in the sorted list until there are no more spots to fit.

Benchmark

Ground truth 3D dataset

The manually annotated 3D dataset (publicly available, see Data Availability section) is composed of three main categories: (i) single-molecule FISH of two genes in *S. cerevisiae*, (ii) mtDNA and mitochondrial network in *S. cerevisiae*, and (iii) COs (tagged COSA-1) in *C. elegans*. The folder structure is compatible with the Cell-ACDC software (*11*) and organized into position folders. The images are in TIFF format, one per channel. Each dataset has been annotated by an expert in each field using Cell-ACDC. The annotations are available in the CSV file ending with "_gt_manual.csv," while the segmentation masks of the cells are available in the file ending with "_segm.npz." Additional details about the dataset are available in table S1.

Methodology

To match predicted spot coordinates with the ground truth annotations, we paired each predicted spot center with the ground truth if they were both inside a spheroid with (3, 4, 4) pixels radii in the (z, y, x) directions centered on the ground truth spot. If multiple predicted spots were found in the spheroid, then only the closest one was paired. The number of paired spots is the number of true positives (TPs), unpaired predicted spots are the false positives (FPs), and unpaired ground truth spots are the false negatives (FNs). We then calculated precision (P), recall (R), and F_1 score (Fig. 2) with the following formulas

$$P = \frac{\mathrm{TP}}{\mathrm{TP}+\mathrm{FP}}; R = \frac{\mathrm{TP}}{(\mathrm{TP}+\mathrm{FN})}; F_1 = \frac{2\mathrm{PR}}{P+R} \quad (5)$$

Parameter selection

To determine the optimal analysis parameters for SpotMAX and RS-FISH (Fig. 2B), we visually selected the parameters that provided the best performance on a few randomly selected z-stacks, and we then ran the analysis with these fixed parameters on the entire dataset. The RS-FISH analysis parameters are reported in table S5. For U-FISH, Piscis, and Spotiflow, we used the default parameters. For Big-FISH, we used the same "voxel_size" and "spot_radius" used in SpotMAX. Python scripts used to run the different methods are available at this repository: https://github.com/SchmollerLab/SpotMAX_benchmark. For Spotiflow 2D in Fig. 2D (left), we used the pretrained "general" model (*2*). For Spotiflow 3D in Fig. 2D (right), we used the pretrained models "synth_3d" and "smfish_3d." To further refine Spotiflow detections, we leveraged SpotMAX's ability to filter true positives based on multichannel numerical features ("+ SpotMAX 3D" in Fig. 2D, right). These features were described and biologically tested in (*16*). Briefly, these are the P value and the t statistic of Welch's t test between the mNeonGreen (mitochondrial nucleoids, spots channel) and mKate2 channels (mitochondrial network, reference channel). The valid spots are those with P value < 0.025 and t statistic > 0. The SpotMAX analysis parameters for each dataset are available in the published dataset (see Data, code, and materials availability in the Acknowledgments section).

COSA-1 experiments in *C. elegans*

Strains

The *C. elegans* strains used for this analysis are the AV630, SMN333, SMN260, SMN350, SMN384, and SMN387. The full genotype of the strains is available in table S4. All strains were maintained at 20°C on nematode growth medium plates with *Escherichia coli* OP50 as previously described (*53*).

New strains for this study were generated by CRISPR-Cas9–mediated genome editing as previously described (*54*). Sequences are listed in table S6. Cas9-NLS protein, trans-activating CRISPR RNA, guide RNAs, and gBlocks to generate repair templates were purchased from IDT, and all oligos were purchased from Sigma-Aldrich. To create the *v5::rad-51(ske48)* allele, we replaced an HA-tag of a *ha::rad-51(ske1)* strain that we generated using a modified Cas9 to recognize a GAG-PAM motif in the N terminus of *rad-51* (table S6).

Cytology and fixed-tissue imaging

Young adult animals were dissected 24 hours after reaching the L4 stage, fixed and stained (GFP::COSA-1 or V5::RAD-51) as previously described (*55*), and mounted in ProLong Glass antifade mounting medium (Invitrogen, P36984). Primary antibodies used for staining GFP and V5 are mouse anti-GFP (Roche, #11814460001) and mouse anti-V5 (Invitrogen, #R960-25), respectively, and the secondary antibody is donkey anti-mouse Alexa Fluor 546 (Invitrogen, #A10036). Halo::COSA-1 was labeled with Janelia Fluor 669 HaloTag ligand (Lavis Lab, JBG-27-075A) (*56*) by feeding as previously described (*57*).

Samples were imaged on an Olympus spinning disk confocal system IXplore SpinSR using a 60× 1.4 numerical aperture oil plan apochromat objective with the cellSens software (Olympus/Evident).

Cell segmentation

Meiotic nuclei were segmented as previously described (*58*) using a custom model (publicly available, see Data, code, and materials availability in the Acknowledgments section). Segmented nuclei were manually checked using Fiji, and only correctly segmented nuclei in late pachytene, marked by the presence of bright COSA-1 spots, were further analyzed by SpotMAX.

S. cerevisiae time-lapse experiments

Yeast strain

The yeast strain FPY004 used in this work is based on W303 and was constructed by crossing the parental strains [yCO380, containing LacO arrays in mtDNA (*16*, *30*)] and ASY014 (*16*). The full genotype is listed in table S3.

Live-cell 4D fluorescence microscopy

The strain FPY004 was grown at 30°C in a shaking incubator at 250 rpm (Infors, Ecotron). Cells were precultured in yeast extract, peptone, and dextrose medium for 6 hours, transferred to SCGal medium (synthetic complete medium containing 2% galactose), and grown for at least 36 hours. The optical density at 600 (OD_{600}) was always kept below

0.5 with a final OD of 0.3. For the live-cell microscopy experiment, 1 ml of culture was sonicated for 3 s and 200 µl was loaded into a CellASIC ONIX2 Y04C microfluidic plate (Merck Millipore) connected to the CellASIC microfluidic pump (Merck Millipore). After trapping the cells in the microfluidic chamber, SCGal medium was continuously supplied with a constant pressure of 13.8 kPa. Image acquisition was performed with a Zeiss LSM 800 confocal microscope (software: Zen 2.3, blue edition); a 63×/1.4 oil differential interference contrast objective; and the Incubator XLmulti S1, Pecon, used to maintain an incubation temperature of 30°C. Cells were imaged for 3 hours, and then the medium was automatically changed to SCD medium (synthetic complete medium containing 2% glucose) and imaged for additional 4.5 hours. The acquisition rate was set to 15 min. Multidimensional imaging was achieved by acquiring 24 z-slices with 0.35 µm spacing for the three channels named T-PMT, mNeonGreen, and mKate2. mKate2 was imaged with an excitation wavelength of 561 nm and detected emission between 610 and 700 nm. mNeon was excited at 488 nm and detected between 410 and 546 nm. Bright-field images were taken using the transmitted light detector (T-PMT). All channels were acquired at the same time.

Cell segmentation, tracking, and cell cycle annotation

All the image analysis steps before SpotMAX analysis were performed with the software Cell-ACDC (*11*). Raw microscopy files generated by the Zeiss microscope were converted into TIFF format using the Bio-Formats library (*59*). Cells were segmented and tracked using YeaZ (*60*) v1.0.3 (embedded in Cell-ACDC) from the bright-field channel. Each time point was then carefully inspected and corrected. The cell cycle annotation was then performed by annotating mother-bud pairing, bud emergence, and cell division. This information was then fed into SpotMAX to count the number of spots (nucleoids) and segment the mitochondrial network in each cell.

Telomere and centromere FISH on HSCs

All work was performed in accordance with the Massachusetts Institute of Technology (MIT) Institutional Animal Care Facility and with guidelines at MIT (Institutional Animal Care and Use Committee) (protocol numbers 0715-073-18 and 0718-053-21). Mice were purchased from the Jackson Laboratory C57BL/6J (#000664).

Murine bone marrow (BM)–derived live G0/1 HSCs (Lin^-, Sca1/$Ly6^+$, CD117/$cKit^+$, CD150/$Slamf1^+$, CD48/$Slamf2^-$, and 7-ADD^-) were isolated as described previously (*31*). Briefly, BM was harvested by flushing the long bones. Red blood cells were lysed in ammonium-chloride-potassium buffer, and samples were washed in Iscove's modified Dulbecco's medium containing 2% fetal bovine serum (FBS). BM cells were resuspended at 10 cells/ml in prewarmed IMEM supplemented with 2% FBS and Hoechst 33342 (6.6 µg/ml; Thermo Fisher Scientific, #H3570). After 45 min of incubation at 37°C in a water bath, cells were washed with cold IMEM with 2% FBS and kept at 4°C. Lineage-positive cells were depleted using a mouse lineage cell depletion kit, and the following antibodies were used for staining: Rat monoclonal phycoerythrin anti-mouse CD150, BioLegend, catalog no. 115904, RRID:AB_313683; Armenian hamster monoclonal APC/Cy7 anti-mouse CD48, BioLegend, catalog no. 103432, RRID:AB_2561463; rat monoclonal APC anti-mouse CD117, BioLegend, catalog no. 105812, RRID:AB_313221; rat monoclonal FITC anti-mouse Ly-6A/E, BioLegend, catalog no. 122506, RRID:AB_756191. An example of the gating strategy is provided in fig. S8.

HSCs were resuspended in PBS and mounted to a well of a four-well chamber slide (MatTek) coated with poly-L-lysine for 1 hour at room temperature. HSCs were then washed with PBS twice for 2 min each time on a slow rocking platform. HSCs were treated with freshly made pepsin solution (0.005% pepsin in 10 mM HCl) before the FISH procedure. The telomere probe [TelC-Alexa488 (target sequence: telomeric CCCTAA repeats)] and centromere probe [CENPB-Cy3 (target sequence: ATTCGTTGGAAACGGGA)] were mixed and diluted to 500 nM per probe, in a hybridization buffer [20 mM tris (pH 7.4), 60% formamide, and 0.5% of Roche blocking reagent (Roche 11096176001)] for hybridization. A 400 µl of diluted probe was used per well (per sample). The rest of the FISH procedure was performed according to the PNA FISH manufacturer's protocol (PNA Bio). The slides were air-dried briefly before being applied with the Prolong Gold Antifade Mountant medium (Thermo Fisher Scientific) and covered with a 1.5 coverslip. The slides were sealed with nail polish and kept in the dark overnight before imaging. An Ultra Deltavision fluorescent microscope with a 60× objective lens (1.4 NA) was used to acquire the images of nuclei with FISH-labeled telomeres and centromeres, under the setting of 1 × 1 binning and a z-stack of 20 slices with 0.75-µm spacing size. During the analysis, we excluded cells that were larger than 2.5 SD than the mean cell size. To analyze HSCs of a specific size, we evaluated the 10% smallest (XS-HSCs), the 10% largest (XL-HSCs) and ±10% HSCs of mean size (M-HSCs). For details about the metric used in Fig. 5D [see the "3D Gaussian fitting procedure (SpotFIT)" section].

Nucleolus and nuclear size analysis in *C. elegans*

Strain

The strain DCW279 was used for this analysis. The full genotype is available in table S4.

Auxin plates and treatment

Auxin (3–indoleacetic acid, Sigma-Aldrich) was dissolved in ethanol to prepare a 57 mM stock solution and stored at 4°C. Auxin was added to NGM plates to a final concentration of 1 mM. Control plates contained an equivalent amount of ethanol (1.75%). Plates were then seeded with OP50 bacteria and let dry.

Embryos isolated by standard hypochlorite treatment were plated onto auxin, or ethanol plates, as control and maintained for 24 hours. Next, the hatched L1 larvae were collected from the plates and imaged.

Microscopy

Microscopy was performed using a confocal spinning disk microscope system from Visitron Systems GmbH, equipped with a Nikon Eclipse Ti2 microscope, a Plan Apo λ 100x/1.45 oil objective, a Yokogawa CSU-W1 confocal scanner unit, a VS-Homogenizer, an EMCCD camera [Andor - iXon Series], and VisiView software for acquisition.

Live microscopy was carried out on 2% agarose pads supplemented with 0.15% sodium azide (Interchim) to paralyze the worms, as previously described (*41*). For each image, a range of 70 to 75 stacks was captured with a z spacing of 200 nm.

Supplementary Materials

This PDF file includes:

Figs. S1 to S9
Tables S1 to S3

REFERENCES

1. E. Bahry, L. Breimann, M. Zouinkhi, L. Epstein, K. Kolyvanov, N. Mamrak, B. King, X. Long, K. I. S. Harrington, T. Lionnet, S. Preibisch, RS-FISH: Precise, interactive, fast, and scalable FISH spot detection. *Nat. Methods* **19**, 1563–1567 (2022).
2. A. Dominguez Mantes, A. Herrera, I. Khven, A. Schlaeppi, E. Kyriacou, G. Tsissios, E. Skoufa, L. Santangeli, E. Buglakova, E. B. Durmus, S. Manley, A. Kreshuk, D. Arendt, C. Aztekin,

J. Lingner, G. La Manno, M. Weigert, Spotiflow: Accurate and efficient spot detection for fluorescence microscopy with deep stereographic flow regression. *Nat. Methods* **22**, 1495–1504 (2025).
3. A. Imbert, W. Ouyang, A. Safieddine, E. Coleno, C. Zimmer, E. Bertrand, T. Walter, F. Mueller, FISH-quant v2: A scalable and modular analysis tool for smFISH image analysis. bioRxiv 453024 [Preprint] (2021); https://doi.org/10.1101/2021.07.20.453024.
4. D. Ershov, M.-S. Phan, J. W. Pylvänäinen, S. U. Rigaud, L. Le Blanc, A. Charles-Orszag, J. R. W. Conway, R. F. Laine, N. H. Roy, D. Bonazzi, G. Duménil, G. Jacquemet, J.-Y. Tinevez, TrackMate 7: Integrating state-of-the-art segmentation algorithms into tracking pipelines. *Nat. Methods* **19**, 829–832 (2022).
5. C. Bentley-Abbot, R. Heslop, C. Pirillo, P. Chandrasegaran, G. McConnell, E. Roberts, E. Hutchinson, A. MacLeod, An easy to use tool for the analysis of subcellular mRNA transcript colocalisation in smFISH data. *Sci. Rep.* **14**, 8348 (2024).
6. B. T. Eichenberger, Y. Zhan, M. Rempfler, L. Giorgetti, J. A. Chao, deepBlink: Threshold-independent detection and localization of diffraction-limited spots. *Nucleic Acids Res.* **49**, 7292–7297 (2021).
7. Z. Niu, A. O'Farrell, J. Li, S. Reffsin, N. Jain, I. Dardani, Y. Goyal, A. Raj, Piscis: A loss estimator of the F1 score enables accurate spot detection in fluorescence microscopy images via deep learning. *Cell Syst.* **16**, 101448 (2025).
8. E. Laubscher, X. Wang, N. Razin, T. Dougherty, R. J. Xu, L. Ombelets, E. Pao, W. Graf, J. R. Moffitt, Y. Yue, D. V. Valen, Accurate single-molecule spot detection for image-based spatial transcriptomics with weakly supervised deep learning. *Cell Syst.* **15**, 475–482.e6 (2024).
9. W. Xu, H. Cai, Q. Zhang, Z. Wang, J. Yang, X. Wu, C. Li, C. Cui, C. Liu, J. He, F. Mueller, J. Dai, C. Hao, W. Ouyang, G. Cao, U-FISH: A fluorescent spot detector for imaging-based spatial-omics analysis and AI-assisted FISH diagnosis. *Genome Biol.* **26**, 261 (2025).
10. B. G. Hospelhorn, B. K. Kesler, H. Jashnsaz, G. Neuert, TrueSpot: A robust automated tool for quantifying signal puncta in fluorescent imaging. *Genome Biol.* **26**, 317 (2025).
11. F. Padovani, B. Mairhörmann, P. Falter-Braun, J. Lengefeld, K. M. Schmoller, Segmentation, tracking and cell cycle analysis of live-cell imaging data with Cell-ACDC. *BMC Biol.* **20**, 174 (2022).
12. BioImage.IO. https://bioimage.io.
13. Y. Sato, S. Nakajima, N. Shiraga, H. Atsumi, S. Yoshida, T. Koller, G. Gerig, R. Kikinis, Three-dimensional multi-scale line filter for segmentation and visualization of curvilinear structures in medical images. *Med. Image Anal.* **2**, 143–168 (1998).
14. D. Chatzitheodoridou, D. Bureik, F. Padovani, K. V. Nadimpalli, K. M. Schmoller, Decoupled transcript and protein concentrations ensure histone homeostasis in different nutrients. *EMBO J.* **43**, 5141–5168 (2024).
15. I. V. Kukhtevich, M. Rivero-Romano, N. Rakesh, P. Bheda, Y. Chadha, P. Rosales-Becerra, S. Hamperl, D. Bureik, S. Dornauer, C. Dargemont, A. Kirmizis, K. M. Schmoller, R. Schneider, Quantitative RNA imaging in single live cells reveals age-dependent asymmetric inheritance. *Cell Rep.* **41**, 11656 (2022).
16. A. Seel, F. Padovani, M. Mayer, A. Finster, D. Bureik, F. Thoma, C. Osman, T. Klecker, K. M. Schmoller, Regulation with cell size ensures mitochondrial DNA homeostasis during cell growth. *Nat. Struct. Mol. Biol.* **30**, 1549–1560 (2023).
17. C. Kukat, C. A. Wurm, H. Spåhr, M. Falkenberg, N.-G. Larsson, S. Jakobs, Super-resolution microscopy reveals that mammalian mitochondrial nucleoids have a uniform size and frequently contain a single copy of mtDNA. *Proc. Natl. Acad. Sci. U.S.A.* **108**, 13534–13539 (2011).
18. D. E. Almanzar, S. G. Gordon, C. Bristow, A. Hamrick, L. von Diezmann, H. Liu, O. Rog, Meiotic DNA exchanges in *C.* elegans are promoted by proximity to the synaptonemal complex. *Life Sci. Alliance* **6**, e202301906 (2023).
19. R. Yokoo, K. A. Zawadzki, K. Nabeshima, M. Drake, S. Arur, A. M. Villeneuve, COSA-1 Reveals Robust Homeostasis and Separable Licensing and Reinforcement Steps Governing Meiotic Crossovers. *Cell* **149**, 75–87 (2012).
20. P. W. Sternberg, K. Van Auken, Q. Wang, A. Wright, K. Yook, M. Zarowiecki, V. Arnaboldi, A. Becerra, S. Brown, S. Cain, J. Chan, W. J. Chen, J. Cho, P. Davis, S. Diamantakis, S. Dyer, D. Grigoriadis, C. A. Grove, T. Harris, K. Howe, R. Kishore, R. Lee, I. Longden, M. Luypaert, H.-M. Müller, P. Nuin, M. Quinton-Tulloch, D. Raciti, T. Schedl, G. Schindelman, L. Stein, WormBase 2024: Status and transitioning to Alliance infrastructure. *Genetics* **227**, iyae050 (2024).
21. J. A. Hollis, M. L. Glover, A. J. Schlientz, C. K. Cahoon, B. Bowerman, S. M. Wignall, D. E. Libuda, Excess crossovers impede faithful meiotic chromosome segregation in *C.* elegans. *PLOS Genet.* **16**, e1009001 (2020).
22. N. Hunter, Meiotic recombination: The essence of heredity. *Cold Spring Harb. Perspect. Biol.* **7**, a016618 (2015).
23. H. M. Ellis, H. R. Horvitz, Genetic control of programmed cell death in the nematode *C.* elegans. *Cell* **44**, 817–829 (1986).
24. Z. Yu, Y. Kim, A. F. Dernburg, Meiotic recombination and the crossover assurance checkpoint in *Caenorhabditis elegans*. *Semin. Cell Dev. Biol.* **54**, 106–116 (2016).
25. B. Schumacher, K. Hofmann, S. Boulton, A. Gartner, The *C.* elegans homolog of the p53 tumor suppressor is required for DNA damage-induced apoptosis. *Curr. Biol.* **11**, 1722–1727 (2001).
26. W. B. Derry, A. P. Putzke, J. H. Rothman, Caenorhabditis elegans p53: Role in apoptosis, meiosis, and stress resistance. *Science* **294**, 591–595 (2001).
27. C. Rinaldo, P. Bazzicalupo, S. Ederle, M. Hilliard, A. La Volpe, Roles for Caenorhabditis elegans rad-51 in meiosis and in resistance to ionizing radiation during development. *Genetics* **160**, 471–479 (2002).
28. B. Galeota-Sprung, A. Fernandez, P. Sniegowski, Changes to the mtDNA copy number during yeast culture growth. *R. Soc. Open Sci.* **9**, 211842 (2022).
29. S.-M. Fendt, U. Sauer, Transcriptional regulation of respiration in yeast metabolizing differently repressive carbon substrates. *BMC Syst. Biol.* **4**, 12 (2010).
30. C. Osman, T. R. Noriega, V. Okreglak, J. C. Fung, P. Walter, Integrity of the yeast mitochondrial genome, but not its distribution and inheritance, relies on mitochondrial fission and fusion. *Proc. Natl. Acad. Sci. U.S.A.* **112**, E947–E956 (2015).
31. J. Lengefeld, C.-W. Cheng, P. Maretich, M. Blair, H. Hagen, M. R. McReynolds, E. Sullivan, K. Majors, C. Roberts, J. H. Kang, J. D. Steiner, T. P. Miettinen, S. R. Manalis, A. Antebi, S. J. Morrison, J. A. Lees, L. A. Boyer, Ö. H. Yilmaz, A. Amon, Cell size is a determinant of stem cell potential during aging. *Sci. Adv.* **7**, eabk0271 (2021).
32. F. Rossiello, D. Jurk, J. F. Passos, F. d'Adda di Fagagna, Telomere dysfunction in ageing and age-related diseases. *Nat. Cell Biol.* **24**, 135–147 (2022).
33. J. Llewellyn, R. Baratam, L. Culig, I. Beerman, Cellular stress and epigenetic regulation in adult stem cells. *Life Sci. Alliance* **7**, e202302083 (2024).
34. R. C. Allsopp, G. B. Morin, J. W. Horner, R. DePinho, C. B. Harley, I. L. Weissman, Effect of TERT over-expression on the long-term transplantation capacity of hematopoietic stem cells. *Nat. Med.* **9**, 369–371 (2003).
35. R. C. Allsopp, S. Cheshier, I. L. Weissman, Telomere shortening accompanies increased cell cycle activity during serial transplantation of hematopoietic stem cells. *J. Exp. Med.* **193**, 917–924 (2001).
36. M. Hultdin, E. Grönlund, K. Norrback, E. Eriksson-Lindström, T. Just, G. Roos, Telomere analysis by fluorescence in situ hybridization and flow cytometry. *Nucleic Acids Res.* **26**, 3651–3656 (1998).
37. M. Guenatri, D. Bailly, C. Maison, G. Almouzni, Mouse centric and pericentric satellite repeats form distinct functional heterochromatin. *J. Cell Biol.* **166**, 493–505 (2004).
38. C. K. Tsang, P. G. Bertram, W. Ai, R. Drenan, X. F. S. Zheng, Chromatin-mediated regulation of nucleolar structure and RNA Pol I localization by TOR. *EMBO J.* **22**, 6045–6056 (2003).
39. L.-W. Lee, C.-C. Lee, C.-R. Huang, S. J. Lo, The nucleolus of Caenorhabditis elegans. *J. Biomed. Biotechnol.* **2012**, 601274 (2012).
40. V. Tiku, C. Jain, Y. Raz, S. Nakamura, B. Heestand, W. Liu, M. Späth, H. E. D. Suchiman, R.-U. Müller, P. E. Slagboom, L. Partridge, A. Antebi, Small nucleoli are a cellular hallmark of longevity. *Nat. Commun.* **8**, 16083 (2017).
41. N. Al-Refaie, F. Padovani, J. Hornung, L. Pudelko, F. Binando, A. del Carmen Fabregat, Q. Zhao, B. D. Towbin, E. S. Cenik, N. Stroustrup, J. Padeken, K. M. Schmoller, D. S. Cabianca, Fasting shapes chromatin architecture through an mTOR/RNA Pol I axis. *Nat. Cell Biol.* **26**, 1903–1917 (2024).
42. S. Sengupta, T. R. Peterson, D. M. Sabatini, Regulation of the mTOR complex 1 pathway by nutrients, growth factors, and stress. *Mol. Cell* **40**, 310–322 (2010).
43. L. Zhang, J. D. Ward, Z. Cheng, A. F. Dernburg, The auxin-inducible degradation (AID) system enables versatile conditional protein depletion in *C.* elegans. *Development* **142**, 4374–4384 (2015).
44. K. Hara, Y. Maruki, X. Long, K. Yoshino, N. Oshiro, S. Hidayat, C. Tokunaga, J. Avruch, K. Yonezawa, Raptor, a Binding Partner of Target of Rapamycin (TOR). *Mediates TOR Action. Cell* **110**, 177–189 (2002).
45. I. V. Kukhtevich, N. Lohrberg, F. Padovani, R. Schneider, K. M. Schmoller, Cell size sets the diameter of the budding yeast contractile ring. *Nat. Commun.* **11**, 2952 (2020).
46. K. L. Sheaffer, D. L. Updike, S. E. Mango, The Target of Rapamycin Pathway Antagonizes pha-4/FoxA to Control Development and Aging. *Curr. Biol.* **18**, 1355–1364 (2008).
47. F. Padovani, T. Stegmaier, B. Mairhörmann, K. M. Schmoller, Analysis of Multidimensional Microscopy Data Using Cell-ACDC. *J. Vis. Exp.* **7**, e68954 (2025).
48. C. Stringer, M. Pachitariu, Cellpose3: One-click image restoration for improved cellular segmentation. *Nat. Methods* **22**, 592–599 (2025).
49. S. Berg, D. Kutra, T. Kroeger, C. N. Straehle, B. X. Kausler, C. Haubold, M. Schiegg, J. Ales, T. Beier, M. Rudy, K. Eren, J. I. Cervantes, B. Xu, F. Beuttenmueller, A. Wolny, C. Zhang, U. Koethe, F. A. Hamprecht, A. Kreshuk, ilastik: Interactive machine learning for (bio) image analysis. *Nat. Methods* **16**, 1226–1232 (2019).
50. M. Weigert, U. Schmidt, Nuclei Instance Segmentation and Classification in Histopathology Images with Stardist in *2022 IEEE International Symposium on Biomedical Imaging Challenges (ISBIC)* (IEEE, Kolkata, India, 2022), pp. 1–4.
51. A. Paszke, S. Gross, F. Massa, A. Lerer, J. Bradbury, G. Chanan, T. Killeen, Z. Lin, N. Gimelshein, L. Antiga, A. Desmaison, A. Köpf, E. Yang, Z. DeVito, M. Raison, A. Tejani, S. Chilamkurthy, B. Steiner, L. Fang, J. Bai, S. Chintala, PyTorch: An Imperative Style, High-Performance Deep Learning Library. arXiv:1912.01703 [cs.LG] (2019).
52. A. Wolny, L. Cerrone, A. Vijayan, R. Tofanelli, A. V. Barro, M. Louveaux, C. Wenzl, S. Strauss, D. Wilson-Sánchez, R. Lymbouridou, S. S. Steigleder, C. Pape, A. Bailoni, S. Duran-Nebreda, G. W. Bassel, J. U. Lohmann, M. Tsiantis, F. A. Hamprecht, K. Schneitz, A. Maizel,

A. Kreshuk, Accurate and versatile 3D segmentation of plant tissues at cellular resolution. *eLife* **9**, e57613 (2020).
53. S. Brenner, The genetics of caenorhabditis elegans. *Genetics* **77**, 71–94 (1974).
54. A. Paix, A. Folkmann, G. Seydoux, Precision genome editing using CRISPR-Cas9 and linear repair templates in *C.* elegans. *Methods* **121–122**, 86–93 (2017).
55. S. Köhler, M. Wojcik, K. Xu, A. F. Dernburg, Superresolution microscopy reveals the three-dimensional organization of meiotic chromosome axes in intact *Caenorhabditis elegans* tissue. *Proc. Natl. Acad. Sci. U.S.A.* **114**, E4734–E7443 (2017).
56. J. B. Grimm, A. N. Tkachuk, L. Xie, H. Choi, B. Mohar, N. Falco, K. Schaefer, R. Patel, Q. Zheng, Z. Liu, J. Lippincott-Schwartz, T. A. Brown, L. D. Lavis, A general method to optimize and functionalize red-shifted rhodamine dyes. *Nat. Methods* **17**, 815–821 (2020).
57. A. R. R. Neves, I. Čavka, T. Rausch, S. Köhler, Crossovers are regulated by a conserved and disordered synaptonemal complex domain. *Nucleic Acids Res.* **53**, gkaf095 (2025).
58. C. Piñeiro López, A. R. Rodrigues Neves, I. Čavka, O. J. Gros, S. Köhler, Segmentation of *C.* elegans germline nuclei. *MicroPubl. Biol.* **2023**, 10.17912 (2023).
59. M. Linkert, C. T. Rueden, C. Allan, J.-M. Burel, W. Moore, A. Patterson, B. Loranger, J. Moore, C. Neves, D. MacDonald, A. Tarkowska, C. Sticco, E. Hill, M. Rossner, K. W. Eliceiri, J. R. Swedlow, Metadata matters: Access to image data in the real world. *J. Cell Biol.* **189**, 777–782 (2010).
60. N. Dietler, M. Minder, V. Gligorovski, A. M. Economou, D. A. H. L. Joly, A. Sadeghi, C. H. M. Chan, M. Koziński, M. Weigert, A.-F. Bitbol, S. J. Rahi, A convolutional neural network se59gments yeast microscopy images with high accuracy. *Nat. Commun.* **11**, 5723 (2020).
61. H. Hofmann, H. Wickham, K. Kafadar, Letter-value plots. *J. Comput. Graph. Stat.* **26**, 469–477 (2017).

Acknowledgments: We thank the Advanced Light Microscopy Facility (ALMF) at the European Molecular Biology Laboratory (EMBL) in Heidelberg, Evident/Olympus, and Zeiss for the support, IT and HPC resources at the European Molecular Biology Laboratory (EMBL) in Heidelberg for providing the essential computational infrastructure, and the Media and Lab Kitchen at the EMBL in Heidelberg for providing media and solutions. Some strains were provided by the CGC, which is funded by the NIH Office of Research Infrastructure Programs (P40 OD010440). We also thank B. Schumacher (University of Cologne) for providing essential *C. elegans* strains for this study. We thank A. Dominguez Mantes from M. Weigert's group at EPFL, Lausanne, for fruitful discussions on how to fine-tune Spotiflow. **Funding:** Work in K.M.S.'s laboratory was supported by the following funding sources: Human Frontier Science Program (career development award to K.M.S), Deutsche Forschungsgemeinschaft (DFG, German Research foundation) through projects 416098229 and 431480687, Helmholtz Association, de.NBI Cloud within the German Network for Bioinformatics Infrastructure (de.NBI) and ELIXIR-DE (Forschungszentrum Jülich and W-de.NBI-001, W-de.NBI-004, W-de.NBI-008, W-de.NBI-010, W-de.NBI-013, W-de.NBI-014, W-de.NBI-016, and W-de.NBI-022), and European Union (ERC, MITOSIZE, 101169998). Views and opinions expressed are however those of the authors only and do not necessarily reflect those of the European Union or the European Research Council. Neither the European Union nor the granting authority can be held responsible for them. Work in S.K.'s laboratory was supported by the following funding sources: European Molecular Biology Laboratory, and Deutsche Forschungsgemeinschaft (DFG, German Research Foundation) project number 452616889. Work in D.S.C.'s laboratory was supported by the following funding sources: Deutsche Forschungsgemeinschaft (DFG, German Research foundation) through projects 459488476 and 507935196. Work in J.L.'s laboratory was supported by the following funding sources: European Research Council, Research Council of Finland, and Swedish Research Council. Work in X.A.S.'s laboratory was supported by the following funding sources: Jane Coffin Childs Memorial Fellowship, Centre for Prostate Disease Research core funding at the Henry Jackson Foundation, and Genitourinary Malignancies Branch of the National Cancer Institute at the National Institutes of Health. **Author contributions:** Conceptualization: F.P., S.K., and K.M.S. Methodology: F.P., I.C., L.B., S.K., and K.M.S. Software: F.P., L.B., T.S., S.K., and I.C. Validation: F.P., I.C., A.R.R.N., N.A.-R., L.B., D.C., Y.C., P.L., T.S., J.L., D.S.C., S.K., and K.M.S. Formal analysis: F.P., I.C., K.M.S., and S.K. Investigation: F.P., I.C., A.R.R.N., N.A.-R., Y.C., X.A.S., J.L., D.S.C., S.K., and K.M.S. Resources: F.P., I.C., A.R.R.N., C.P.L., N.A.-R., Y.C., X.A.S., J.L., D.S.C., S.K., and K.M.S. Data curation: F.P., I.C., A.R.R.N., N.A.-R., L.B., D.C., Y.C., P.L., T.S., X.A.S., J.L., D.S.C., S.K., and K.M.S. Writing—original draft: F.P., S.K., and K.M.S. Writing—review and editing: F.P., I.C., A.R.R.N., C.P.L., N.A.-R., L.B., D.C., Y.C., P.L., T.S., X.A.S., J.L., D.S.C., S.K., and K.M.S. Visualization: F.P. and K.M.S. Supervision: F.P., S.K., K.M.S., and D.S.C. Project administration: F.P., S.K., and K.M.S. Funding acquisition: K.M.S., J.L., D.S.C., S.K., and X.A.S. **Competing interests:** The authors declare that they have no competing interests. **Data, code, and materials availability:** The code needed to run the models tested in Fig. 2 (A to D) is publicly available at the permanent repository at https://zenodo.org/records/21309745 or on the GitHub page (https://github.com/SchmollerLab/SpotMAX_benchmark). The manually annotated 3D dataset is publicly available at the permanent repository (https://doi.org/10.6019/S-BIAD3750). SpotMAX source code is available at the permanent repository (https://doi.org/10.5281/zenodo.21285537) or on the GitHub page (https://github.com/SchmollerLab/SpotMAX). Cell-ACDC source code is available at the permanent repository (https://doi.org/10.5281/zenodo.6631113) or on the GitHub page (https://github.com/SchmollerLab/Cell_ACDC). The custom model used to segment the nuclei in Fig. 3 is publicly available at the permanent repository at https://zenodo.org/records/21309934 or the GitHub page (https://github.com/KoehlerLab/Cellpose_germlineNuclei/blob/main/Cellpose_germlineNuclei/cellpose_germlineNuclei_KoehlerLab), and it is available through Cell-ACDC (with automatic download). All *C. elegans* and *S. cerevisiae* strains generated for this study are available upon request to the corresponding authors [francesco.padovani@helmholtz-munich.de (F.P.); simone.koehler@embl.de (S.K.); kurt.schmoller@helmholtz-munich.de (K.M.S.)].

Submitted 30 January 2025
Accepted 15 July 2026
Published 28 August 2026
10.1126/sciadv.adw3811

ScienceAdvances

SpotMAX: A generalist framework for multidimensional automatic spot detection and quantification

Francesco Padovani, Ivana #avka, Ana Rita Rodrigues Neves, Cristina Piñeiro López, Nada Al-Refaie, Leonardo Bolcato, Dimitra Chatzitheodoridou, Yagya Chadha, Pablo Lagos, Timon Stegmaier, Xiaofeng A. Su, Jette Lengefeld, Daphne S. Cabianca, Simone Köhler, and Kurt M. Schmoller

Sci. Adv. **12** (35), eadw3811. DOI: 10.1126/sciadv.adw3811